TÉCNICO LISBOA

Transformers for Contactless Power Supplies in High Voltage Lines

Francisco Martins Farinha Barata Serrano

Thesis to obtain the Master of Science Degree in

Electrical and Computer Engineering

Examination Committee

Chairperson: Prof. Doutora Maria Eduarda de Sampaio Pinto de Almeida Pedro
Supervisor: Prof. Doutor José Fernando Alves da Silva
Co-supervisor: Prof. Doutora Maria José Ferreira dos Santos Lopes de Resende
Member: Prof. Doutor José Henrique Querido Maia
Member: Prof. Doutor Elmano da Fonseca Margato

November 2013

Agradecimentos

O meu sincero reconhecimento para com o meu orientador, Professor Doutor José Fernando Alves da Silva e co-orientadora, Professora Doutora Maria Jose Ferreira dos Santos Lopes de Resende. As suas ajudas concedidas durante o desenrolar desta dissertação foram determinantes para a conclusão do trabalho. Por fim, desejo agradecer todo o apoio e carinho que recebi da minha família, em especial dos meus pais e irmão.

Resumo

O sistema eléctrico de transmissão de energia da maioria dos países desenvolvidos está a envelhecer e a ficar sujeito a uma carga cada vez maior, o que aumenta o numero de falhas nos equipamentos. Tal facto diminuiu a fiabilidade do sistema, incrementando os custos de operação e diminuindo a qualidade de serviço. Por sua vez, a expansão da rede está constrangida, pelo que a possível solução para o problema é optimizar o funcionamento e melhorar a inspecção e manutenção do sistema existente.

A utilização de robots de inspecção autónomos em planos de inspecção e manutenção de linhas de transmissão é uma opção recente para esta tarefa, que reduz os custos e aumenta a segurança dos trabalhadores [1–3]. A fonte de alimentação do robot foi identificada como um componente crucial na viabilidade do projecto.

Desenvolvimentos recentes determinaram, favoravelmente, a viabilidade de uma fonte de alimentação suportada no campo magnético que é gerado em torno da linha de transmissão. Acresce que esta solução possui vantagens significativas em relação a outras possibilidades como proporcionar ao robot uma fonte de energia que o torna independente por longos períodos de tempo [4, 5]. Para utilizar a energia proveniente do campo magnético é colocado um transformador que envolve o cabo e funciona como um transformador de corrente [3, 6].

O objectivo desta dissertação é desenvolver modelos de dimensionamento que são adequados à especificidade do transformador de corrente, contribuindo para uma maior precisão dos resultados. É feita uma análise sistemática deste tipo de transformador e são apresentados vários modelos que em seguida são validados com ensaios em carga de transformadores construídos num recente trabalho nesta area [7]. Para além disso, é também ligado um condensador ao transformador para injectar uma corrente desmagnetizante e com isso aumentar a potência de saída que é transferida para a carga. São estabelecidos procedimentos de dimensionamento e por fim são efectuados ensaios em carga com e sem condensador para quantificar o impacto do mesmo.

Palavras Chave

Ensaios em carga, Manutenção de linhas de transmissão, Modelos de dimensionamento, Núcleo Magnético, Transformador de corrente, Circuito ressonante

Abstract

The electrical transmission system of most developed countries is ageing and under increasing load, which gives rise to equipment wear-out failures. This diminishes system reliability and increases the global cost of operation. Since the grid is constrained to expand, a possible solution is to optimize the operation and improve the inspection and maintenance of the existing power system. Through such process the goal is to maximize utilization, boost efficiency and enhance reliability of the transmission network.

The use of autonomous robots in inspection and maintenance plans of overhead transmission lines is a valid option to achieve such a task while minimizing costs and ensuring worker safety. The power supply of the robot has been identified has a crucial component in the viability of the project.

Recent developments have determined that a power supply based on the magnetic energy around the power transmission line is feasible and possesses significant advantages over known options, such as enabling the robot to operate unattended for long periods of time and permitting weight reduction of the power supply. To use the magnetic energy, a current driven transformer is clamped around the power line, functioning mechanically alike a current probe [3, 6].

The purpose of this thesis is to develop adequate design models for this current driven transformer and contribute to more accurate results. A systematic analysis of this current transformer is given, and various computer design models are presented and validated against extensive experimental load tests carried out in transformers that were built during the course of a recent work in the area.

Furthermore, a capacitor is connected to the transformer secondary in order to establish a resonant circuit and therefore increase the output power transferred to the load without increasing the size of the core. Design procedures for this case are displayed and related to computer simulation. Load tests are presented and compared with the case without the capacitor.

Keywords

Current transformer, Load tests, Magnetic core, Power line maintenance, Resonant circuit, Transformer design models

Contents

List of Figures

List of Tables

Nomenclature

Note that time varying voltage, current and flux are denounced by the use of lower-case symbols. Upper-case symbols of voltage, current and flux express the magnitude of the variable in question.

A_c	*Effective cross section of the core,* m^2
A_p	*Area product,* m^4
A_t	*External surface area,* m^2
A_{wp}	*Primary wire area,* m^2
A_{ws}	*Secondary wire area,* m^2
ϕ	*Magnetic flux,* Wb
Ψ	*Magnetic flux linkage,* Wb
λ	*Induction leakage coefficients,* Wb
B	*Magnetic flux density,* T
B_r	*Residual magnetic flux density,* T
B_s	*Saturation magnetic flux density,* T
B_{ac}	*Maximum magnetic flux density of operation,* T
C	*Capacitance,* F
c_v	*Core volume,* m^3
η	*Efficiency*
emf	*Electromotive force,* V
f	*Frequency,* Hz
γ	*Density,* kg/m^3
H	*Magnetic field intensity,* A/m

H_c	*Magnetic field required to return flux to zero,* A/m
H_s	*Magnetic field at saturation,* A/m
ID	*Inner diameter,* m
i_m	*Magnetizing current,* A
i_p	*Primary current,* A
i_s	*Secondary current,* A
J	*Current density,* A/m^2
k	*Magnetic link factor*
K_L	*Transformer load factor*
K_f	*Waveform coefficient*
K_s	*Stacking factor*
K_u	*Window utilization factor*
l_c	*Core length,* m
l_g	*Air-gap length,* m
L_{l_p}	*Primary inductance,* H
L_M	*Mutual inductance,* H
L_{l_s}	*Secondary inductance,* H
L_m	*Magnetizing inductance,* H
MLT	*Mean Length Turn,* m
M_{PL}	*Magnetic Path Length,* m
mmf	*Magnetomotive force,* ampere-turn
μ	*Permeability*
μ_r	*Relative permeability*
μ_e	*Effective permeability*
μ_0	*Permeability of vacuum,* $4\pi \times 10^{-7}$ H/m
OD	*Outer diameter,* m
N_p	*Primary turns*
N_s	*Secondary turns*

P_i	*Input power,* W
P_o	*Output power,* W
P_p	*Primary copper loss,* W
P_s	*Secondary copper loss,* W
P_{cu}	*Copper loss,* W
P_{fe}	*Core loss,* W
P_Σ	*Total loss,* W
R_p	*Resistance of the primary winding,* Ω
R_s	*Resistance of the primary winding,* Ω
R_c	*Equivalent resistance representing core loss,* Ω
R_o	*Load resistance,* Ω
$\mathcal{R}$	*Magnetic reluctance,* A-turns/Wb
ρ	*Wire resistivity,* Ω·m
S_t	*Total transformer apparent power,* VA
Γ	*Dissipated power per surface area,* W/cm^2
T_r	*Temperature rise above* $20\ ^o$C, ^{o}C
t_c	*Core width,* m
v_p	*Primary voltage,* V
v_s	*Secondary voltage,* V
W_a	*Window area,* m^2
W_t	*Total transformer weight,* kg
W_{tcu}	*Copper weight,* kg
W_{tfe}	*Iron weight,* kg
X_p	*Primary reactance,* Ω
X_s	*Secondary reactance,* Ω
X_m	*Magnetizing reactance,* Ω
Z_ϕ	*Exciting branch impedance,* Ω

Terms

AC	*Alternating Current*
AISI	*American Iron and Steel Institute*
CRGO	*Cold Rolled Grain Oriented*
CRNO	*Cold Rolled Non Oriented*
DC	*Direct Current*
D-FACTS	*Distributed Flexible AC Transmission Systems*
RIOL	*Robotic Inspection Over Power Lines*
rms	*Root Mean Square*

1

Introduction

1.1 Context and State of the Art

Power utility companies in most of the developed countries are facing the problem of operating and maintaining electrical transmission systems that are ageing and under increasing load, whilst being constrained to expand the grid [10, 11]. The process of ageing gives rise to equipment wear-out failures and the increased demand for electricity results in congestions, significantly increasing the stress-related faults. Hence, future system reliability is diminished and the global cost of operation is increased, not only from constraints in total power transfer capacity but also from the required expansion, redundancy and added maintenance plans. Typically, these are the industry practices, yet the inherent high costs of equipment and labour, as well as time-frame, associated to the planning and construction of high voltage lines have impaired such solutions. Also, the growing public sentiment against locating new transmission power lines in the communities is an important deterrent.

Given that the modern way of life and industrial infrastructure needs an ever-growing amount of affordable and reliable electricity [12], it's clear that power utility companies are forced to maximize utilization, efficiency and enhance reliability of the existing transmission system. This critical issue must be implemented while minimizing operation and maintenance costs, in order to avoid a significant increase in the price of electricity.

To achieve such a task, possible options are the use of autonomous robots in inspection and maintenance plans of overhead transmission lines [1–3] and the use of Distributed Flexible Alternate Current Transmission Systems (D-FACTS) to control power flows in the transmission grid [8, 13]. Figure 1.1 shows a conceptual schematic for each of these solutions.

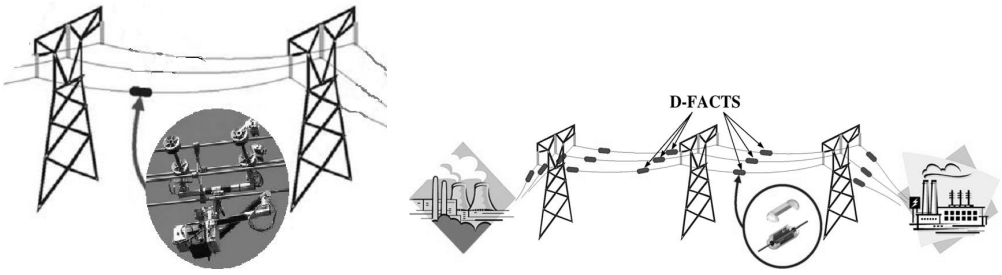

(a) Transmission line inspection robot. (b) D-FACTS deployed on power line (source: [8]).

Figure 1.1: Schematic concept of RIOL and D-FACTS.

Of the various approaches to D-FACTS devices, the distributed series impedance is seen as the most simple and cost effective while providing an higher reliability [13]. A typical series device implementation injects an impedance or voltage that realizes a variable line impedance, which helps control the active power flow in a given transmission line, providing means to solve congestions in the power grid. As perceived in Figure 1.1(b), the D-FACTS modules are placed along the overhead line and use a two parts core transformer that clamps to the line conductor forming a complete magnetic circuit. When activated, the transformer is used either to directly

modify the total line impedance by injecting the magnetizing inductance, or in other approaches, to feed an inverter that will inject a quadrature voltage into the power line to simulate a positive or negative inductance.

The inspection and maintenance of high voltage overhead power lines is a complex and costly large-scale operation which conventionally involves highly trained personal making use of helicopters coupled with high-end sensors and detection systems. Ensuring worker safety is also an extremely relevant concern given the hazardous characteristics of the job, thus a significant amount of funds are allocated to protection equipment and to a premium wage for workers. A fully autonomous robot that slowly navigates along power lines while performing inspection, monitoring and maintenance tasks is a viable alternative to the conventional methods. Furthermore, it can also perform a much more thorough inspection over long periods of time, increasing the overall cost effectiveness and accuracy of the process [1].

One of the main issues that has been a barrier for implementing the line inspection robot is its power supply system. A myriad of options have been proposed and investigated, either as standalone or cooperative sources: small-size gasoline operated generator; high capacity batteries; embedded wind or photovoltaic power systems that feed a battery pack; harvesting power from the magnetic or electric field generated by the high voltage transmission line. Since full autonomy is a key factor when assessing the economical advantages of this type of robot against typical inspection strategies and due to the specific environment were the robot is operating, some of the referred options can be discarded. Weight to power ratio is also an exclusion factor, given that the robot's expected power consumption is in the 1 kW range and total weight must be kept at a reasonable limit imposed by the line infrastructure [3, 14].

Therefore, as demonstrated in [1], the gasoline powered generator is troublesome because of noise, the need for a choke in cold days, lack of a fuel tank that can be inclined and a short lifespan that would require maintenance every half year. The sole use of high capacity batteries is undesirable, since weight to power ratio rises sharply, even at the current state of the art battery technology, limiting the autonomy of a robot with a viable weight to a couple of hours. Photovoltaic and wind power systems coupled with a battery pack are infeasible considering that both rely on intermittent power sources to charge the battery, which depend on various non-controllable weather factors, thus crippling autonomy [4]. Furthermore, the dimensions and characteristics of the equipment required in both systems would unbalance the robot in case of wind gusts [15].

A solution based on the concept of harnessing power from the created magnetic or electrical field of the inspected high voltage line can devise a durable power supply method for the robot [5, 16]. This option has potential to provide full autonomy, enabling the robot to perform inspection over long distances of live lines without interruptions. Hence, this solution presents a clear advantage over the other referred technologies.

Initial research in the area of harvesting power from high voltage transmission line as shown that devices making usage of the generated electrical field don't yield enough power to suppress the robot's power consumption [4]. For a device of approximately the size of an power line marker, the expected power captured is about 0.5 W. The obtained value, coupled with the dimensions of the required equipment, indicates that the weight to power ratio is inadequate, given that the robot's power needs are around 1 kW and the total weight of the power supply must be kept at around 10 kg. Hence, this would dictate a rather voluminous power supply apparatus with complex mechanical considerations to properly take advantage of the static induction [5, 16].

On the other hand, preliminary studies on usage of the magnetic field created by a transmission line to power the autonomous inspection line robot, while it operates along the line, have demonstrated that enough energy can be obtained to serve the power demanded by the robot [6, 14]. Albeit this solution explicitly needs current flowing through a phase line, the value of such current can vary in a wide range of operation, from low load to peak load situations of the power system, without significant prejudice to the robot power supply [14].

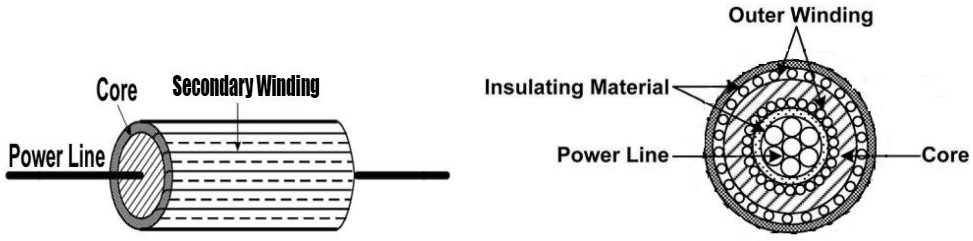

(a) Single-turn coaxial transformer. (b) Front view of the transformer.

Figure 1.2: Scheme of transformer used to retrieve power from the magnetic field of a transmission line (source: [8]).

In order to retrieve power from the magnetic field due to a current flow through the line, this contactless power transfer approach resorts to a transformer as exemplified in Figure 1.2. The closed magnetic circuit is achieved using two separate halves made of magnetic material that are physically joined together around the line conductor, forming the transformer core.

The power line is guided through the core and acts as the primary winding of the transformer as seen in Figure 1.2(a). A outer secondary winding with multiple turns is then wound on the core, thus completing the transformer circuit of which a front cut view is presented in Figure 1.2(b). This configuration enables movement of the core and secondary winding in respect to the power line conductor.

Furthermore, exploiting the electromagnetic induction presents interesting mechanical advantages since the resultant device has a compact shape that can be seamlessly integrated into one of the robot arms/clamps, making it easy to attach and detach from the power line [3, 17]. This has minimal impact on the balance of the robot during maneuvers as well as it's stability during harsh weather conditions.

A power supply relying on the magnetic field created by the transmission line can easily accommodate and charge a battery pack which further extends the Robotic Inspection Over Power Lines (RIOL) unattended operation and maneuver capabilities during various possible situations [14]. Notice that while overcoming obstacles in a transmission line (such as towers, aviation markers, insulators and other possible obstructions) the clamp containing the transformer is opened [3], effectively opening the magnetic circuit and switching off energy harvesting, hence the power needed for these maneuvers must be provided by small onboard batteries.

If the transmission line current drops to a critical value or when the line has to be switched off, the robot can enter a hibernation status until nominal line current is restored. Thought this situation is an exception, since normally a transmission line has continuous circulation current for economic reasons and system operation purposes. Recognizing this fact further enables the optimization of the battery pack, reducing it's size and weight considerably.

As concluded throughout different projects in the field of D-FACTS and RIOL, the transformer is identified as being a crucial element in the success of the implementation [6, 8, 14, 16]. Careful design steps have to be taken into account since the effects of the magnetization current and core saturation are significantly reflected on output power [7]. In addition, at each step, several physical restrictions must be complied. These include a maximum allowed weight and volume, plus other considerations, as for example, a minimum core window area must be established to contain the line conductor and the wound secondary.

Another relevant aspect lies in the choice of ferro-magnetic materials, since weight and volume are to be kept at the lowest possible whilst achieving the targeted output power. Most implementations have relied on silicon-steel which is the industry standard for transformers operating in the 50 Hz range. Relatively to other available materials it offers high maximum operating flux, high permeability and is cost-effective [9].

For the RIOL, the design procedure of the required transformer is based on the principle of operation that characterizes a current transformer [6]. From the magnetic field created by a current in the transmission line that is guided through the core, an electromagnetic induced voltage is developed through the secondary winding. The corresponding current feeds a power rectifier which enables energy transfer to the robot. A newly developed power supply incorporates a control scheme for the switching rectifier that presents the power supply circuit as a slowly varying resistance to the transformer secondary winding terminals [14].

A recent work implemented various transformers with UI shaped laminations [7] and UU shaped cores [7] made of silicon steel. Output power measurements yielded up to 600 W and concluded that enough power can be obtained given a suitably sized ferro-magnetic core wound with sufficient turns to match the load specifications. Additionally, short and open circuit tests coupled with impedance measurements suggest that performing further field testing will contribute to a more precise modelling of the relevant phenomena in order to achieve a design procedure.

1.2 Objective

The main goal of this thesis is to further investigate and test the possible solutions for contactless power supplies in high voltage lines. The transformers designed and tested are prototypes of what is destined to equip a RIOL robot.

There has been previous work in this field as seen in [7], hence the task is also to continue and expand such work through improvements in the circuit models and design procedures as well as promoting further experimental testing of the transformers.

New circuit models for the RIOL transformer must be developed with a focus on considering more non-idealities associated to a real transformer. As a result, distinct expressions for the output power of the transformer are expected along with insight concerning the influence of considering leakage flux in the model.

A thorough examination and extensive laboratory evaluation of the transformers developed in [7] is to be performed and the results matched against theoretical values that will originate from the new models that are part of the aim of this thesis. A resonant circuit is also being tested in order to enhance the output power of the transformers.

1.3 Thesis organization

This thesis is organized in the following way:

- **Chapter 2 -** Presents the fundamental magnetic and electrical principles that govern the transformer. Magnetic permeability is also defined along with the relevant $B - H$ loop. The concept of the magnetic circuit is applied to define the representation of a real transformer.
- **Chapter 3 -** Describes the specifications and the design process of a transformer suitable for the RIOL. The magnetic materials available are discussed in detail. Circuit models for the RIOL transformer are developed. A design algorithm is presented and discussed.
- **Chapter 4 -** The transformers used throughout this thesis are described in this chapter. Each transformer is presented in detail and key specifications are discussed. Physical and electrical specifications are enumerated for each individual transformer.
- **Chapter 5 -** Explains the laboratory set-up and evaluates the transformers through a series of tests. Performance under load operation is assessed and comparison with theoretical values is established for each transformer. A resonant circuit, based on a capacitor, is also experimented.
- **Chapter 6 -** Closes this thesis with a revision of the developed work and the conclusions that can be extracted from it. In addition, various topics for future analysis and implementation are also enumerated.

2

Transformer theory

The fundamental magnetic and electrical principles that describe the transformer are presented in this chapter. Electromagnetism is applied to express the relation between induced electromotive force and magnetic flux as described by Faraday's law in the transformer operation principle. Magnetomotive force is derived through Ampere's law as reflected in the net ampere-turns acting on the transformer circuit. An analogous relationship is made with electrical circuits which forms Hopkinson's law that relates flux and magnetic resistance or reluctance with the magnetomotive force. Magnetic permeability is used to relate magnetic field intensity with magnetic flux density. The typical magnetization path for materials that form the core of a transformer is presented. The effects of hysteresis and saturation are also shown. A first approximation is applied to reach a linear relationship between magnetic field intensity and magnetic flux density.

A simplifying assumption involves the concept of the magnetic circuit. Essentially, this is based on the fact that the transformer core consists of a high permeability material that channels almost all of the magnetic flux created in the circuit. The expressions that define an ideal transformer are established under certain conditions. The conditions expressed by the ideal transformer laws are approached, but never realized in physical transformers. Finally, this chapter explains the origins of transformer losses and presents the concept of an equivalent circuit that addresses each non-ideality present in real transformers.

2.1 Magnetic and Electrical Fundamentals

Transformers are electrical devices that change or transform the amplitude of voltage and current in two or more circuits. The transformer is a static device and, therefore, the power transferred between circuits is almost the same, apart from typically small losses. Hence, the transformer presents a relatively high efficiency from a common 95% and upwards to 99%.

The operating principle of a transformer is based on inductive coupling. That is, when a varying magnetic flux links a circuit, an electromotive force or voltage, is induced in the circuit. A simple application of this principle is observed in Figure 2.1, were a alternating current in the primary winding creates a varying magnetic flux, thus producing a varying magnetic field through the secondary winding. In turn, the varying magnetic field induces a varying electromotive force across the secondary winding terminals. This effect liberates electrical energy transfer between the primary winding to the inductively coupled secondary winding.

Notice that, while part of the total flux establishes a mutual flux that links both windings, a fraction of the produced flux only links one of the windings. This is known as leakage flux and doesn't contribute to inductive coupling, since it only links one winding without linking the other. Leakage flux is normally a small fraction of the total flux, but it's influential in the behaviour of a transformer. Optimizing the placement of the windings reduces leakage flux and thus mitigates the detracting effect on transformer operation. A common practice is to physically place the primary and secondary windings as close together as possible, by subdividing them into sections.

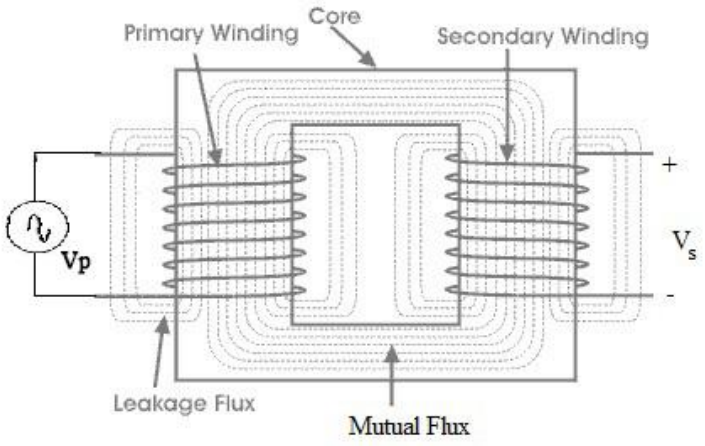

Figure 2.1: Transformer functioning principle (source: [9]).

As an electrical and magnetic circuit, the transformer's phenomena of interest is governed by a set of laws attributed to Maxwell, Faraday and Ampere. The relationships between electromotive force (*emf*), flux (ϕ) and magnetic flux density (B) are given by Faraday's law. Magnetomotive force (*mmf*), magnetic field intensity (H) and electrical current (i) are interleaved through the application of Ampere's law. The unifying ground of the expressions retrieved from these laws is defined by the medium characteristics of the magnetic core, in which a mutual flux is established.

The schematic transformer in Figure 2.1 demonstrates an alternating voltage being applied to the primary winding, while keeping the secondary circuit opened. An alternating current flows in the primary and forms an alternating magnetic field around the primary circuit, which creates a mutual flux that links both circuits and induces an *emf* given through Faraday's law [18]. Considering the directions marked in Figure 2.5, the *emf* can be expressed as:

$$emf_p = N_p \frac{d\phi}{dt} \tag{2.1}$$

The established *emf* counters the applied voltage and balances the primary voltage together with the voltage drop associated to the current flowing in the primary winding. Since most power transformers present a very small no-load voltage drop, the induced emf_p nearly equals the applied voltage v_p, thus the voltage drop in the primary resistance is typically disregarded:

$$v_p = emf_p + R_p i_\phi \rightarrow v_p \cong emf_p \tag{2.2}$$

Expression (2.2) is only valid while neglecting leakage flux, since considering it would add an additional induced *emf* term to the equation. Given the approximation already being made by neglecting the primary resistance voltage drop and knowing that leakage flux is normally a small percentage of the total flux, then writing (2.2) is valid to describe power transformer operation.

The current that flows through the windings corresponds to the net ampere-turns acting on the magnetic circuit, constituting the exciting current. A resultant magnetomotive force is derived from the application of Ampere's law along a closed path [18]:

$$mmf = \sum_{k=1}^{n} N_k i_k \tag{2.3}$$

This suggests that the magnetomotive force in magnetic circuits is analogous to electromotive force in electrical circuits. The analogy can be further extended to magnetic flux being similar to current, as it also forms a closed loop as described by Maxwell's equations. A empirical corollary rises in the form of Hopkinson's law, that is analogous to Ohm's law for a magnetic circuit [18]:

$$mmf = \phi \mathcal{R} \tag{2.4}$$

Therefore, the magnetomotive force is related to the current flowing through a winding or to the flux that is developed inside a element that presents a "resistance" to the flowing of magnetic flux. This "resistance" is a characteristic of the medium and is denominated magnetic reluctance. A magnetic field causes magnetic flux to follow the path of least magnetic reluctance. A poor conductor of flux has a high magnetic reluctance and will require a higher *mmf* to obtain a given magnetic flux as expressed in (2.4). Since magnetic flux always forms a closed loop and follows the path of least reluctance, the concentration of flux in a given area will depend on the reluctance of the material placed in that area and its surroundings. Hence, the coupling between two windings is more efficient in proportion to the lesser magnetic reluctance of the chosen core, as it establishes a confined alternating mutual flux.

In the schematic of Figure 2.1 the core material was made of air, an air-core, hence the magnetic reluctance would be high which is a characteristic of the air. Accordingly, a weak coupling will be established function of the low valued mutual flux. On that account, there is a need to choose a closed-loop medium that features a relatively low magnetic reluctance to enable a stronger coupling and thus more efficient energy transfer. Typically, a iron core or other ferromagnetic material is selected to provide a confined path linking the windings. Figure 2.2 exposes two diagrams demonstrating the usage of a magnetic core in a transformer circuit.

A continuous magnetic core is presented in Figure 2.2(a), in this case the magnetic reluctance will be constant along the magnetic path covered by the established flux. However, most magnetic circuits are not continuous and usually contain a small air gap in addition to the path in the core as shown in Figure 2.2(b). When a air gap or other material discontinuities exist in the core, the magnetic reluctance of Figure 2.2(b) is evaluated as a combination (serial or parallel) of the magnetic reluctances of the various paths along the magnetic core.

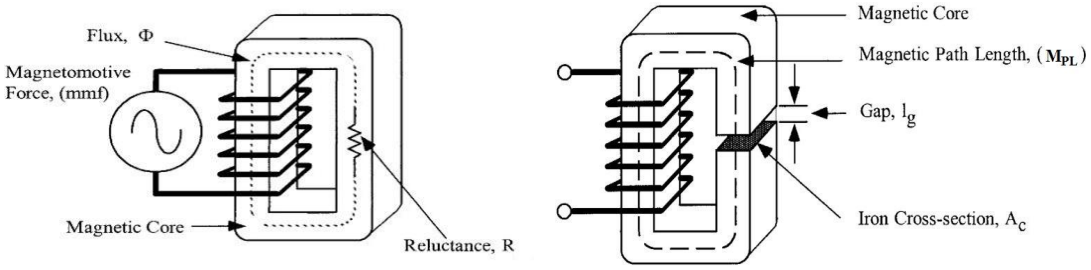

(a) Magnetic Core. (b) Magnetic Core with air gap.

Figure 2.2: Typical magnetic core schemes (source: [9]).

If the cross-sectional area of the magnetic core is considerer constant along the magnetic path, then the magnetic reluctance, $\mathcal{R}$, of a continuous core can be defined as [18]:

$$\mathcal{R} = \frac{M_{PL}}{\mu_o \mu_r A_c} \tag{2.5}$$

Therefore, magnetic reluctance is function of the core magnetic path length, M_{PL}, covered by the magnetic flux and inversely proportional to the product of the core cross-section, A_c, with the effective magnetic permeability, $\mu_o \mu_r$, of the medium. Hence, for a given magnetic path length and core cross-section, a material with high permeability will have a low magnetic reluctance. For the case of Figure 2.2(b), the magnetic reluctance associated with the air gap, $\mathcal{R}_g$, is:

$$\mathcal{R}_g = \frac{l_g}{\mu_o A_c} \tag{2.6}$$

which is valid if fringing in the air-gap is neglected. Consequently, the total magnetic reluctance of the magnetic core, $\mathcal{R}_t$, can be defined as the sum of (2.5) and (2.6) along their respective path length:

$$\mathcal{R}_t = \frac{M_{PL}}{\mu_r \mu_o A_c} + \frac{l_g}{\mu_o A_c} \tag{2.7}$$

For the geometry under consideration, a more generic form of (2.4) is based on the empirical conclusion that a magnetic circuit can be approximated by homogeneous sections of length l_k, each having a defined magnetic reluctance in which a portion of the total flux circulates. Therefore, magnetomotive force is the series or parallel association of the n^{th} terms composed of a section's reluctance and channelled magnetic flux [18]:

$$mmf = \sum_{k=1}^{n} \phi_k \mathcal{R}_k = \sum_{k=1}^{n} \phi_k \frac{l_k}{\mu_k \mu_o A_c} \tag{2.8}$$

The net magnetic flux through a magnetic component is proportional to the number of magnetic field lines that pass through the cross sectional area of that component. If the magnetic flux density, B, is considered uniform across the core cross-section, A_c, of the magnetic circuit of Figure 2.2, then the flux, ϕ, is given by [18]:

$$\phi = BA_c \tag{2.9}$$

For a magnetic circuit with a similar geometry to the one presented in Figure 2.2, it is reasonable to assume that the magnetic flux density, B, is constant in the core cross-section and the magnetic path length of any flux line is close to a mean core length M_{PL}. Under these assumptions, the magnetic field, H, is merely the total magnetomotive force divided by the length of the magnetic path [18]:

$$H = \frac{mmf}{M_{PL}} = \frac{\sum_{k=1}^{n} N_k i_k}{M_{PL}} \tag{2.10}$$

2.2 Magnetic Permeability

As stated, transformer theory is interleaved through the characteristics of the material in which the magnetic core is built. The relationship is established by defining magnetic permeability as the interaction between the magnetic field intensity, H, and the magnetic flux density, B, whilst being a intrinsic property of a material. In essence, permeability is the ability that a material has to conduct flux, therefore, easily magnetized materials such as iron have high magnetic permeability.

For a given magnetic material under alternating sinusoidal operation, the magnetic flux density traced against the magnetic field intensity results in a cyclic magnetization process as represented in Figure 2.3(a). It can be observed that magnetic circuits are non-linear, suffering from saturation and hysteresis, that is, the present state of a ferromagnetic material depends on its past magnetic history. Several key points are shown in Figure 2.3(a). The dotted line represents the magnetization curve, an idealized curve that assumes the magnetic material is completely demagnetized and is then subjected to a gradually increasing magnetic field until saturation is achieved. This point is signalled by the maximum flux density B_s and maximum magnetic field intensity H_s. As the magnetic field is lowered from H_s to zero, the remaining induction left in the material is B_r.

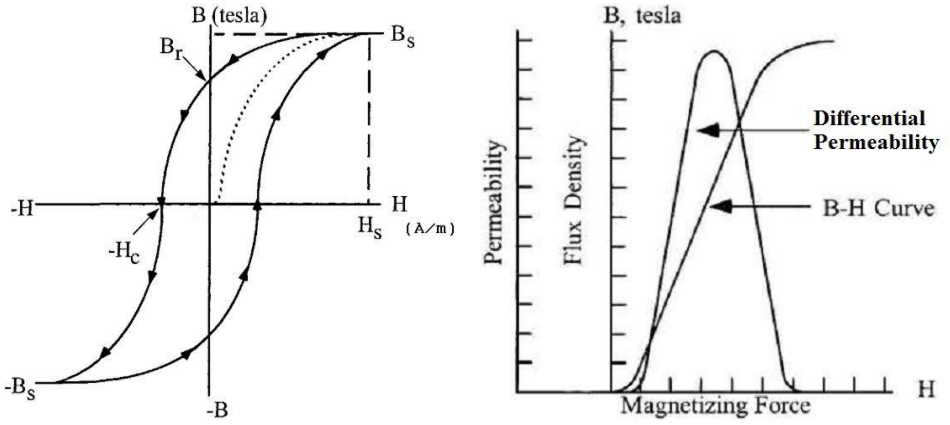

(a) Typical hysteresis loop. (b) Permeability along the magnetization curve.

Figure 2.3: Hysteresis cycle and variation of permeability (source: [9]).

Further lowering the field to the coercive magnetic field, H_c, reaches a point were magnetic flux density is nullified. Because the loop is symmetrical about the origin, it has corresponding points on the opposite side. Thus, the cycle is repeated according to the frequency of operation, but without going through the magnetization curve because of the residual magnetic field density. It is also important to acknowledge that the area enclosed by the hysteresis loop is the magnetic energy per unit volume and per cycle dissipated in hysteresis processes.

Figure 2.3(b) reveals the variation of the magnetic differential permeability along the magnetization curve. Inspecting it shows that maximum permeability occurs reasonably below saturation, B_s, of the magnetic material. As the material is brought to saturation, the permeability decreases sharply, signifying the inability to retain a higher flux density for an increasing magnetic field.

Therefore, permeability is not constant, having its value defined as the measure of the achieved magnetic flux density for a given magnetic field. Consequently, the reluctance of a magnetic circuit expressed in (2.5) is also not constant, but varies depending on the magnetic field and inversely to magnetic permeability [18].

At any point on a magnetization path, the ratio of B to H is denominated ratio permeability, while the slope of the curve at the given point is called the differential permeability. Henceforth, for practical purposes, it is convenient to assume a linear relationship B-H characteristic for high permeability materials [9]:

$$B = \mu H \tag{2.11}$$

were $\mu = \mu_o \mu_r$. The value of μ_r for air is 1, whereas for soft iron materials μ_r is around 4000. Since the magnetic flux density of operation in power transformer cores should be kept below saturation in normal operations to avoid high exciting currents, the effects of saturation are hardly noticeable, and the core can be assumed to have a constant single value permeability.

The above is applicable to a continuous magnetic core as seen in Figure 2.2(a). If an air-gap is introduced, with the configuration of Figure 2.2(b), the magnetic permeability is affected and the

influence of the gap must be accounted for. In such cases, effective permeability can be derived by using the magnetic circuit approximation:

$$\mu_e = \frac{l_g + M_{PL}}{\frac{l_g}{\mu_o} + \frac{M_{PL}}{\mu_o \mu_r}}, \text{ if } l_g << M_{PL} \implies \mu_e = \frac{\mu_o \mu_r}{1 + \mu_r \left(\frac{l_g}{M_{PL}}\right)} \tag{2.12}$$

Inspection of (2.12) reveals that introducing a small air gap into the magnetic path will significantly lower the core permeability by a factor related to ratio between the length of the magnetic path and the length of the air-gap. Thus, the B-H loop of Figure 2.3(a) will be sheared along the magnetic field intensity axis, that is, a higher value of magnetic field is now necessary to achieve the same magnetic flux density. In practical terms this stabilizes the magnetic core to changes in applied winding voltage, frequency and temperature.

2.3 Ideal Transformer

Consider the case of a single phase ideal transformer circuit in order to establish the fundamental voltage and current transformation relationships. Figure 2.1 resembles the representation of an ideal transformer with a primary winding of N_p and a secondary winding of N_s turns.

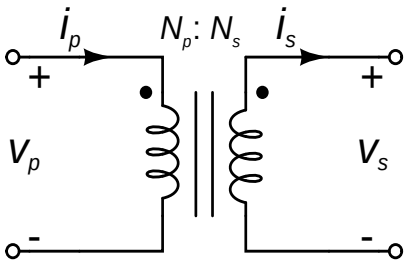

Figure 2.4: Ideal transformer circuit.

The following assumptions and simplifications are done to describe the ideal transformer operation [18]:

- All flux generated is confined to the core and the primary is perfectly linked to the secondary. Flux leakage is neglected since all flux is mutual.
- The respective winding resistances associated with the primary and secondary are disregarded;
- *mmf* is omitted since core permeability is set sufficiently high to establish flux with a residual exciting current.

With a zero mean value alternating voltage applied to the primary of the transformer introduced in Figure 2.4, and abiding to the above assumptions, a varying core flux is established and thus

a *emf* is induced across the primary winding. The core flux will then link the primary to the secondary and induce a *emf* in the secondary winding.

Relating back to (2.1) and (2.2) dictates that both *emf* developed in the primary and secondary winding will equal their respective terminal voltage. The induced *emf* is proportional to the number of turns linked by the changing flux. Thus, when two circuits are linked by a common flux and have different linked turns, different voltages will be induced:

$$v_p = \textit{emf}_p = N_p \frac{d\phi}{dt} \tag{2.13}$$

$$v_s = \textit{emf}_s = N_s \frac{d\phi}{dt} \tag{2.14}$$

a voltage transformation ratio can then be expressed by the ratio of (2.13) and (2.14):

$$\frac{v_p}{v_s} = \frac{N_p}{N_s} \tag{2.15}$$

Since *mmf* is negligible, it can be verified from (2.4) that the magnetic reluctance of the core approaches zero. Consequently a flux is established while the exciting current is close to zero, hence the net *mmf* remains unchanged since the primary winding *mmf* balances the secondary *mmf*. Therefore, applying (2.3) returns:

$$N_p i_p - N_s i_s = 0 \implies N_p i_p = N_s i_s \tag{2.16}$$

a current transformation ratio can then be expressed directly in the form:

$$\frac{i_p}{i_s} = \frac{N_s}{N_p} \tag{2.17}$$

thus the current is transferred by the reciprocal of the ratio by which the voltage is transformed.

In accordance with the ideal transformer assumptions, all the dissipative and energy storage of the transformer have been nullified. Consequently, the input power submitted to the primary will be extracted as output power in the secondary. The conservation of instantaneous power in the ideal transformer is verified by matching (2.15) to (2.17):

$$v_p i_p = v_s i_s \tag{2.18}$$

The transformation ratios of (2.15) and (2.17) enable a voltage or current to be written in terms of a voltage or current from the opposite side of the ideal transformer. By deduction, an impedance connected to either side of the ideal transformer can be transferred indistinguishably from one side to the other. Hence, an impedance connected to the secondary winding can be replaced by an equivalent impedance in the primary winding by means of:

$$\frac{\bar{V}_p}{\bar{I}_p} = \left(\frac{N_p}{N_s}\right)^2 \frac{\bar{V}_s}{\bar{I}_s} \implies \bar{Z}_p = \left(\frac{N_p}{N_s}\right)^2 \bar{Z}_s \tag{2.19}$$

which demonstrates that impedances are transformed in the direct ratio squared.

2.4 Non-idealities

The ideal transformer representation of section 2.3 is unfit for detailed transformer performance analysis. Therefore, the departures of realizable transformers from the ideal transformer must be taken into account. This can be accomplished by applying theory of magnetically coupled circuits to achieve a mathematical model, or by means of equivalent circuit techniques that exercise convenient approximations to translate physical concepts towards a quantitative theory [18].

All of the assumptions made for the ideal transformer are set aside and a corresponding non-ideality arises to better model the physical phenomena of interest. These include the effects of leakage fluxes, winding resistances and a core with finite magnetic permeability that also bears non-linear behaviours.

Stray capacitances associated with varying potentials of closely spaced primary and secondary windings are neglected since the transformers analysed in this thesis operate at a steady-state 50 Hz frequency. Moreover, there is no need to cover rapid changing transient conditions.

A single phase transformer equivalent circuit is presented in Figure 2.5. It can be seen as an ideal transformer with external impedances that are each linked to a non-ideality or loss.

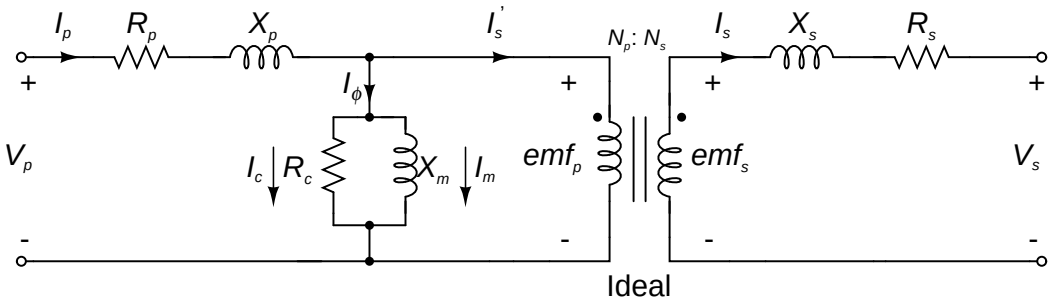

Figure 2.5: Transformer equivalent circuit.

Primary and secondary windings are made of conductors that have a finite conductivity, thus presenting a resistance to the flow of current. The value of the primary and secondary winding resistances is respectively:

$$R_p = \rho \frac{MLT_p}{A_{wp}} N_p \qquad\qquad R_s = \rho \frac{MLT_s}{A_{ws}} N_s \tag{2.20}$$

where ρ represents the resistivity of the wire material, normally copper or aluminium, at the temperature of interest. Expression (2.20) is valid if the total resistance is considered as the DC resistance, that is, the effects of AC current on resistance are disregarded. This approximation is typically valid when using small wire sizes or stranded and transposed cables.

Because the permeability of the core is finite, there will always be some flux that leaks from the core, even without any load current. Leakage flux is thus the contribution of all flux in the spaces around and between the conductors that flows out of the core through empty space.

Total leakage flux can be divided into primary and secondary leakage, that is, the amount of flux that links only one winding and doesn't contribute to the resultant mutual flux. Since leakage flux travels mostly through empty space, instead of through iron, there is no hysteresis or saturation and the permeability in this region is a constant equal to μ_0. Therefore, the induced voltage created by leakage flux varies linearly with current and the leakage-flux linkages with the primary or secondary can be represented by a leakage inductance. The associated leakage reactance of the primary and secondary windings is given by:

$$X_p = 2\pi f L_{l_p} \qquad\qquad X_s = 2\pi f L_{l_s} \tag{2.21}$$

The fundamental component of the exciting current, I_ϕ, can be decomposed into two components known as the core-loss component, I_c, which is in-phase with emf_p and the magnetizing component, I_m, which is lagging emf_p by 90^o.

As for the core-loss component, it accounts for the power absorbed by eddy currents and hysteresis loops. Eddy currents occur because ferromagnetic materials are themselves conductors, hence, the changing flux in the core sets up small current loops that represent power loss which is independent of load current. The continuous alignment and reversal of particles in the core, which give the core its magnetic properties, is another source of power loss by the transformer core known as hysteresis loss.

Hysteresis and eddy current losses form the core or iron loss. Since the current associated with the core loss, I_c, is in addition to the transformed load current, $I_s^{'}$, the core loss can be represented by a resistance, R_c, in parallel with the primary of the ideal transformer. The value of the resistance will vary with the operating conditions of the transformer. However, these losses are, to a good approximation, proportional to the square of the magnetic flux density and hence, they are also proportional to the square of the voltage across the core. Thus, the value of the resistance can be approximated to the following expression [18]:

$$R_c = \frac{emf_p^2}{P_{fe}} \tag{2.22}$$

The magnetizing component, I_m, is required to produce flux and is added to the transformed input current. It does not represent an active power loss, therefore it can be accounted for by an inductance, L_m, in parallel with the ideal transformer. Any non-linear effects, due to ferromagnetic materials, are represented by changes in this inductance. When the core is operating sufficiently below saturation, core non-linearity effects can also be ignored and L_m is constant [18]. The corresponding magnetizing reactance is given by:

$$X_m = 2\pi f L_m \tag{2.23}$$

In the equivalent circuit of Figure 2.5, the parallel combination of R_c and X_m constitutes the excitation branch. When R_c is assumed constant and under sine wave operation, the core loss varies as $\phi_{max}^2 f^2$, where ϕ_{max} is the maximum value of the resultant mutual flux.

Since the magnetizing reactance, X_m, varies with the saturation of the iron, the magnetizing current is assumed to be independent of frequency and directly proportional to the resultant mutual flux when X_m is deemed constant [18].

The current transformation for a ideal transformer (2.17) neglects the current which flows in the primary independent of the load current. By inspecting Figure 2.5, one can observe that the primary current, I_p, must comply with two purposes: magnetize the core, through I_m, and provide current to the load connected to the secondary, through $I_s^{'}$ [18]. Hence, the primary current must generate the necessary *mmf* to yield the resultant mutual flux and, in addition, counteract the effect of the secondary *mmf* which acts to demagnetize the core. This notion leads to the following current relationship in the transformer circuit:

$$\begin{aligned} N_p I_m &= N_p I_p - N_s I_s \\ &= N_p(I_m + I_s^{'}) - N_s I_s \Rightarrow I_s^{'} = \frac{N_s}{N_p} I_s \end{aligned} \tag{2.24}$$

Terminal voltages, V_p and V_s in Figure 2.5, are not the induced voltages developed in the transformer windings *emf*$_p$ and *emf*$_s$, respectively. This occurs because of the associated winding resistances and the created leakage flux that does not couple both transformer windings. This is accounted for in the equivalent circuit by the voltage drops across R_p and R_s as well as on leakage reactances X_p and X_s presented on each winding. Hence, the voltage transformation is established by the resultant mutual flux that links both windings and thus dictates that the induced voltage ratio must equal the winding turns ratio:

$$\frac{\textit{emf}_p}{\textit{emf}_s} = \frac{N_p}{N_s} \tag{2.25}$$

It's implicit in expressions 2.24 and 2.25 that the transformed voltages and currents are always less than the value predicted by the turns ratio because of losses. Furthermore, these also enable to refer all quantities of the primary or secondary of the equivalent circuit to one side of the ideal transformer represented in Figure 2.5. Typically, all quantities of the secondary are referred to the primary side by the use of:

$$R_s^{'} = \left(\frac{N_p}{N_s}\right)^2 R_s \qquad\qquad X_s^{'} = \left(\frac{N_p}{N_s}\right)^2 X_s \tag{2.26}$$

A transformer with two windings and a finite permeability iron core denotes an interesting magnetic non-ideality that is a direct consequence of the fact that only a portion of the developed total flux generates mutual flux between the windings [18]. In this case the total flux, Ψ_p and Ψ_s, is divided in two parcels. The first is the mutual flux, $\Psi_{p,m}$ and $\Psi_{s,m}$, which goes through the core and links both primary and secondary winding. The second is called leakage flux, $\Psi_{p,\lambda}$ and $\Psi_{s,\lambda}$, and goes through air linking only one winding. This notion leads to the following set of equations regarding each winding:

$$\begin{cases} \Psi_p = \Psi_{p,m} + \Psi_{p,\lambda} \\ \Psi_s = \Psi_{s,m} + \Psi_{s,\lambda} \end{cases} \tag{2.27}$$

The mutual linkage flux terms presented in expression (2.27) can be written in regard to the number of turns of the primary and secondary windings and the mutual flux that links them as:

$$\begin{cases} \Psi_{p,m} = N_p \phi \\ \Psi_{s,m} = N_s \phi \end{cases} \tag{2.28}$$

where ϕ is expressed from applying (2.3) and (2.8) with the result:

$$\phi = \frac{N_p i_p - N_s i_s}{\frac{M_{PL}}{\mu_r \mu_o A_c}} \tag{2.29}$$

Flux leakage field lines travel predominantly through air and therefore are not subject to magnetic saturation [18]. This indicates that there is a linear relationship between flux leakage, $\Psi_{p,\lambda}$, $\Psi_{s,\lambda}$, and the respective winding current, i_p, i_s, which leads to the concept of induction leakage coefficients, λ_p, λ_s, in the form of:

$$\begin{cases} \Psi_{p,\lambda} = \lambda_p i_p \\ \Psi_{s,\lambda} = \lambda_s i_s \end{cases} \tag{2.30}$$

In the case of disregarding leakage flux, the equivalent circuit self and mutual inductances of expressions (2.21) and (2.23) can be obtained from decomposing the terms of (2.28):

$$l_{l_p} = \frac{N_p^2}{\frac{M_{PL}}{\mu_r \mu_o A_c}} \tag{2.31}$$

$$L_M = \frac{N_p N_s}{\frac{M_{PL}}{\mu_r \mu_o A_c}} \tag{2.32}$$

$$l_{l_s} = \frac{N_s^2}{\frac{M_{PL}}{\mu_r \mu_o A_c}} \tag{2.33}$$

For the complete solution, with leakage flux considered, (2.27) can be transformed using the results from (2.30)-(2.33) to achieve the following expressions [18]:

$$\begin{cases} \Psi_p = (l_{l_p} + \lambda_p) i_p - L_M i_s \\ \Psi_s = (l_{l_s} + \lambda_s) i_s - L_M i_p \end{cases} \tag{2.34}$$

that denotes the general form of the self and mutual inductances represented in the equivalent circuit of the two winding transformer with iron core:

$$L_{l_p} = l_{l_p} + \lambda_p \tag{2.35}$$

$$L_M = L_m \frac{N_p}{N_s} \tag{2.36}$$

$$L_{l_s} = l_{l_s} + \lambda_s \tag{2.37}$$

Finally, with flux leakage taken into account, it is possible to write a factor expressed through the self and mutual inductances that represents the strength of the magnetic link factor created in the transformer [18]:

$$k = \frac{L_M}{\sqrt{L_{l_p} L_{l_s}}} < 1 \tag{2.38}$$

2.5 Power losses

A real transformer is not lossless from a power transfer point of view due to losses. These are typically divided into two types: copper losses, P_{cu}, and iron or core losses, P_{fe}. The difference between input power and output power is converted into heat, which dictates a direct relationship between efficiency, regulation and temperature rise [18]. Transformer efficiency is thus written as:

$$\eta = \frac{P_o}{P_i} = \frac{P_o}{P_o + P_\Sigma} \tag{2.39}$$

where, for a pure resistive load, the relations are $P_i = V_s I_s$, $P_o = V_s I_s$ and $P_\Sigma = P_{cu} + P_{fe}$.

Copper loss is a variable loss that is related to the current demand of the load. It increases by the square of the current and therefore is deemed a quadratic loss [18]. Relating to the circuit of Figure 2.5, the total copper loss for a single phase two winding transformer is given by:

$$P_{cu} = P_p + P_s = R_p I_p^2 + R_s I_s^2 \tag{2.40}$$

and can be rewritten in terms of input apparent power, S_t, efficiency, η, and the transformer load factor, K_L, as:

$$P_{cu} = \frac{S_t(1-\eta)}{\eta(1+K_L^2)} \tag{2.41}$$

The core loss is a fixed loss closely related to the properties of the material in which the core is built [18]. The energy is dissipated in the core and can be divided into two types: hysteresis losses and eddy current losses. Eddy current loss is caused by circulating currents in the magnetic core, which arise from voltages induced by the changing flux in the core.

A precise calculation of the hysteresis and eddy current losses in a transformer is a complex task that is typically approximated by resorting to empirical data collected from the manufacturer of the core or lamination. Core loss is thus given by the expression [9]:

$$P_{fe} = \text{[W/kg]} \cdot W_{tfe} \tag{2.42}$$

where the term $[W/kg]$ is the rated power loss per kilogram of a given material operating at a certain frequency and subjected to a set magnetic flux density. This concept will be discussed more thoroughly in Chapter 3 along with several other core material details.

3

Transformer design

In this chapter the specifications and the design process of a transformer suitable to supply the RIOL are presented. Transformers are the largest, heaviest, and often costliest of circuit components. They perform fundamental functions in electrical systems as diverse as the power grid or mobile phones. Consequently, they are designed for specific requirements, as optimum performance over a wide range of operation is not offered.

The high cost of transformers is due to the difficulty of standardization, the materials needed, and the processes inherent in their manufacture. The geometry of the magnetic circuit is three-dimensional which places a fundamental restraint on reducing transformer size. Furthermore, the properties of available materials further limit weight reduction.

Firstly, a summary of the requirements for the robot's transformer are exposed. Afterwards, the magnetic materials of choice are described and compared among each other to reach a valid solution for the transformer core. Silicon steel is then discussed in more detail with the specific properties of the various laminations that are available in the industry. Core loss is more thoroughly explained and a core loss equation is presented.

The next step is developing transformer design models that are suitable for the representation of the RIOL transformer. A design algorithm is then presented based on the models developed coupled with geometry considerations that are specific for the various possible transformer cores.

3.1 General specifications

A transformer designed to equip the RIOL must comply with a set of specifications that are necessary to achieve a valid implementation of the power supply. The most significant requirements to take into account while designing the transformer are:

- Operate at 50 Hz to match the transmission line frequency;
- Deliver up to 1 kW in order to meet the power needs of the RIOL;
- Manage oscillations in the transmission line current, therefore being able to accommodate sufficient power transfer throughout the 100 A to 1000 A range of the 220 kV transmission line. This will enable operation in both low load and peak load situations of the power system;
- Feed the RIOL at a constant DC voltage of 55 V;
- Its desirable to have an uniform distribution of the magnetic field inside the transformer core, this dictates a cylindrical shape
- Relatively low weight, around 7 kg, since the total weight of the RIOL must be kept at a reasonable limit imposed by the line infrastructure. Weight to power ratio is an important exclusion factor;
- Small volume and with a compact shape in order to have minimal impact on the balance of the robot during maneuvers and while facing harsh weather conditions;
- As low as possible total cost. This is greatly determined by the material of choice, hence a cost-benefit approach must be employed while excluding ferro-magnetic materials.
- A temperature rise of less than $30\ ^{o}$C above ambient temperature should be observed in the transformer core in order to maintain safety of the equipment and enhance durability of the transformer parts.

3.2 Transformer core materials

The choice of the magnetic material is one of the most important aspects in the design of a transformer core suitable for the RIOL. This will imply a design trade-off between cost, size and performance. In broad terms, the choices available for this work are: silicon steel, nickel iron (permalloy), cobalt iron (supermendur), amorphous metallic alloys, and ferrites. A choice will arise from this group of magnetic materials based on the specific magnetic properties of each material and their adaptation to the design requirements. Amorphous metallic alloys and ferrites can be excluded from the start since they are more geared towards high frequency applications and are costly to produce [9].

In order to pinpoint the best possible choice of material, it is necessary to apply cost and size constraints in conjunction with a series of magnetic properties that define performance. These properties are: saturation B_s, permeability μ_r, resistivity ρ, remanence B_r and coercivity H_c.

As shown in Figure 2.3(a), saturation is a point where further increasing H does not cause useful increase in B. The higher the saturation point of a material, the better capability of it carrying more flux and thus increase induced voltage through Farady's law. Higher permeability materials will present a lower reluctance core that in turn concentrates flux lines and enables a lower leakage flux. Higher electrical resistivity materials oppose induced voltages caused by the changing flux and therefore reduce eddy currents inside the core, effectively reducing core losses. Referring back to Figure 2.3(a), by inspection, it can be seen that lowering the remanence and coercivity values will shrink the area enclosed in the hysteresis loop and consequently reduced hysteresis losses as a lower amount of energy is needed while changing magnetic domains.

Table 3.1: Typical properties of iron alloy magnetic materials (source: [9]).

Material	Composition	B_s [T]	B_r [T]	H_c [A/m]	μ_r	Core Loss [W/kg]	γ [g/cm^3]
Silicon Steel	97% Fe 3% Si	1,8	1,4	39,8	4000	0,85 at 1,5 T 50 Hz	7,63
Supermendur	51% Fe 49% Co	2,2	2,1	15,9	2000	2,08 at 2,0 T 50 Hz	8,15
Orthonol	50% Fe 50% Ni	1,3	1,1	11,9	7500	0,14 at 1,0 T 50 Hz	8,24
Permalloy	20% Fe 80% Ni	0,8	0,6	3,9	4700	0,02 at 0,6 T 50 Hz	8,73

Among the ferromagnetic elements of commercial interest, the most widely used in the industry are iron, nickel and cobalt. Iron is the most plentiful and is alloyed to produce magnetic steels with enhanced properties. Nickel alloys are expensive and typically left for high performance devices. Cobalt is the most scarce and expensive and it's alloys possess valuable magnetic properties. Typical values for the magnetic properties of interest of Silicon Steel, Supermendur, Orthonol and Permalloy are presented in Table 3.1. Resistivity is represented through core loss at a point of operation, since it is more accurate to determine the suitability of a material by knowing it's behaviour at the frequency of interest and at a rated magnetic flux density.

Figure 3.1 shows typical DC hysteresis loops for iron alloys, namely, Silicon Steel 3.1(a), Supermendur 3.1(b), Orthonol 3.1(c) and Permalloy 3.1(d). It can be seen that all the materials possess relatively low remanence flux as well as low coercive force, therefore they can be deemed *soft*, as opposed to *hard* materials that are more suitably used as permanent magnets. *Soft* materials are required by devices which develop alternating fields.

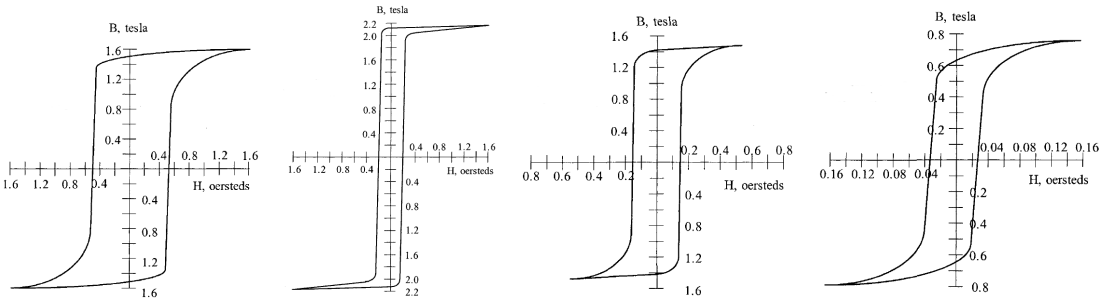

(a) Silicon Steel. (b) Supermendur. (c) Orthonol. (d) Permalloy.

Figure 3.1: Typical DC hysteresis loops for iron alloys (source: [9]).

The main design requirements of the material for use in the transformer equipping the RIOL are: high magnetic flux density, high permeability, low core loss at high magnetic flux density and 50 Hz coupled with low density due to weight restrictions and high availability/low cost.

By inspecting Table 3.1 it can be seen than Silicon Steel offers a compromise between high flux density and core losses. It should be noted that Orthonol and Permalloy offer lower core loss but at significantly lower flux density, while Supermendur has a higher flux density but also relevant core loss in comparison to Silicon Steel.

In terms of permeability, Orthonol and Permalloy show the highest value, but due to significantly higher cost and low availability they pale in direct comparison with Silicon Steel and therefore are more geared towards high performance devices where the need for their special properties justifies the cost. Supermendur is characterized by half the permeability of Silicon Steel and as a consequence is of less interest, with the added factor of being extremely costly.

As for density, Silicon Steel denotes the lowest value of the group and in that regard is more suitable for the transformer equipping the RIOL since weight is a restriction.

Silicon Steel is widely used for operation at power frequencies ($50/60$ Hz), while Supermendur, Orthonol and Permalloy are more resorted to in the audio frequency (around 400 Hz) since they present considerably lower core losses relatively to other materials at that frequency range.

A decision is made by making the normal design trade-off study: cost, size, and performance. Silicon steel offers high saturation flux density, a relatively good permeability at high flux density, and a moderate loss at the frequency of interest. The slight drawback being a higher coercive force than the other materials at disposal. In addition, Silicon Steel is less dense and by far the most available and less costly of the group. All things considered, the material of choice for the transformer equipping the RIOL is Silicon Steel.

3.2.1 Silicon Steel

Silicon steel is the most widely used soft magnetic material. The addition of silicon to iron reduces hysteresis loss, increases magnetic permeability and electric resistivity, thus reducing eddy current losses. The presence of silicon has the disadvantage that the steel becomes brittle and hard so that, for reasons of workability and ease of core manufacture, the quantity must be limited to about 4,5 %. Modern electrical steels have a silicon content of about 3%. The elimination of impurities, including carbon, also has a significant effect in the reduction of losses.

The properties of magnetic materials are affected by the composition of the material, by the way the material is fabricated, and by the heat treatment of fabricated parts. Silicon steel is milled in thin sheets with varying thickness. The thickness of the sheet and the rolling process used to form the sheet affect magnetic properties. These are then restored and enhanced through heat treating after fabrication.

One of the important improvements made to the silicon steel was in the process called cold-rolled, grain-oriented (CRGO). This grain-oriented steel has exceptionally low losses and high permeability. It is used in applications requiring high performance and the losses will be at a minimum. The relative permeability for a magnetic flux density reasonably below saturation is so high that the initial curve is close to the B axis if B versus $\mu_0 H$ is plotted in the SI system. In addition, the hysteresis loops are very narrow and closely hug the initial curve, denoting the low hysteresis loss.

Silicon steel alloys are made in a number of different grades, thicknesses, and surface treatments accompanied by various rolling and annealing processes. Nowadays each manufacturer has it's own grading system and the AISI classification was dropped as a consequence. The magnetic properties of various commonly used laminations are gathered in Table 3.2. Note that all of these have a composition of 97% Fe and 3% Si.

Table 3.2: Magnetic properties of silicon steel laminations (source: [9]).

Thickness [mm]	B_s [T]	B_r [T]	H_c [A/m]	μ_r	Core Loss [W/kg]	Type
0,05	1,9	1,4	39,79	3980	1,66 at 1,5 T 50 Hz	CRGO
0,10	1,9	1,4	31,83	3980	1,25 at 1,5 T 50 Hz	CRGO
0,30	1,9	1,4	7,96	3980	1,37 at 1,5 T 50 Hz	CRGO
0,35	1,9	1,4	7,96	3980	0,85 at 1,5 T 50 Hz	CRGO
0,47	1,9	1,4	39,79	795	1,93 at 1,5 T 50 Hz	CRNO
0,63	1,9	1,4	47,75	795	4,51 at 1,5 T 50 Hz	CRNO

When designing magnetic components, core loss is a major design factor. The core loss is a function of the magnetic material, thickness, magnetic flux density, frequency and temperature. Hence, core loss can be controlled by selecting the right material with the appropriate thickness.

Core loss is made up of two components: the first, the hysteresis loss, is proportional to the frequency and dependent on the area of the hysteresis loop, which, in turn, is a characteristic of the material and a function of the peak flux density; the second is the eddy current loss which is dependent on frequency but is also directly proportional to the the thickness of the material.

In practice the eddy current term is a complex one and can itself be considered to consist of two components: the first truly varies with frequency, material thickness and flux density, thus being referred to as the classical eddy current loss. The second is dependent of the structure of the material such as grain size and magnetic domain movement during the magnetising cycle and is known as anomalous loss or residual loss. Anomalous eddy current loss can account for around half the total no load loss for any particular steel.

Minimising hysteresis loss thus depends on the development of a material having a minimum area of hysteresis loop, whilst minimising eddy current loss is achieved by building up the core from a stack of thin laminations and increasing resistivity of the material in order to make it less easy for eddy currents to flow.

Although some manufacturers supply performance data in the form of curves showing typical properties as functions of such variables as frequency, f, magnetic flux density and temperature, it has become common to present core loss in the form of an equation such as:

$$\text{[W/Kg]} = k_{cl} f^{(m)} B^{(n)} \tag{3.1}$$

where the coefficients k_{cl}, m and n are given in Table 3.3 for each lamination thickness.

Table 3.3: Core loss coefficients for silicon steel laminations (source: [9]).

Thickness [mm]	Frequency [Hz]	k_{cl}	(m)	(n)
0,02	50 to 60	0,059300	0,993	1,740
0,05	50 to 60	0,005970	1,260	1,730
0,10	50 to 60	0,003570	1,320	1,710
0,30	50 to 60	0,001490	1,550	1,870
0,35	50 to 60	0,000557	1,680	1,860
0,60	50 to 60	0,038600	1,000	2,092

Cold rolled grain-oriented steel (CRGO) is usually supplied by the producing mills in coil form and it has to be cut into laminations which are then used to form a transformer core, which is an integral part of any transformer. Grain-oriented steel is used in large power and distribution transformers, and certain audio output transformers.

Cold rolled non-oriented steel (CRNGO) is less expensive than CRGO, and is used when cost is more important than efficiency, and for applications where the direction of magnetic flux is not constant, as in electric motors and generators with moving parts.

A careful selection of the correct material, and operating within its limits, will prevent overheating that could result in damage to the wire insulation and/or the potting compound. Inspecting Table 3.2 reveals that a lamination of $0,35$ mm wields the most favourable core loss figure while being relatively less costly than thinner laminations.

If higher core loss is deemed acceptable as a design trade-off with cost, then the lamination of $0,47$ mm is a valid option, albeit the inherent value of magnetic permeability is significantly lower than other thinner laminations.

3.3 Design models

Note that from this point on the circuit analysis is considered for the particular case of an applied sinusoidal voltage to the primary. The result of integrating Faraday's law, (2.1), for an applied sine wave voltage, yields an expression that relates the maximum magnetic flux density, B_{ac}, and the cross-sectional area of a transformer, A_c, with the applied $(\textit{rms})$ voltage on either side of the transformer $V_{p,s}$:

$$B_{ac} = \frac{V_{p,s}}{K_f A_c N_{p,s} f} \tag{3.2}$$

where the wave form coefficient for sinusoidal wave forms has the value of $K_f = 2\pi/\sqrt{2}$.

An expression for the total apparent power, S_t, handled by the transformer can then be derived by multiplying both sides of expression (3.2) with the primary current expression $I_p = JW_aK_u$, were J is the current density established in the conductor and K_u is the window utilization factor which relates the effective area occupied by the windings with the window area of the transformer:

$$S_t = K_f K_u B_{ac} J f A_c W_a \tag{3.3}$$

A standard method of transformer core selection is based on the window area product by choosing a core that has a window area product equal or larger to the calculated value. The power handling capacity of a transformer core can be determined by the product of available core window area, W_a, and effective core cross-sectional area, A_c, of the transformer:

$$A_p = A_c W_a = \frac{2S_t}{K_f K_u B_{ac} J f} \tag{3.4}$$

Introducing laminations for minimizing eddy current loss increases the cross-section of the core since laminations are coated with a thin insulation layer. This effect is quantified by means of a stacking factor, K_s, defined as:

$$K_s = \frac{\text{volume of iron}}{\text{volume of iron} + \text{volume of insulation}} \tag{3.5}$$

3.3.1 No leakage flux and optimum load

A first approximation of modelling the transformer and the RIOL is to consider the options described in [7]. These consisted in disregarding both the winding resistances as well as the hysteresis and eddy current losses, while assuming no leakage flux is present.

The transformer is thus reduced to the magnetizing component represented by an inductance, L_m, in parallel with the ideal transformer. It is also assumed that the core is operating sufficiently below saturation, hence core non-linearity effects can also be ignored and L_m is constant. The RIOL power supply is accounted for by an optimum resistive load in parallel with the secondary winding. Figure 3.2 shows the equivalent circuit for this case.

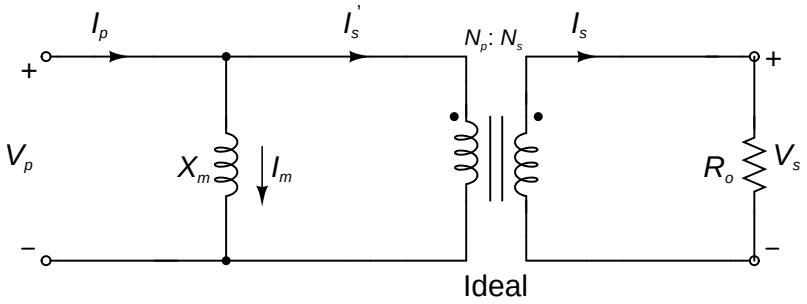

Figure 3.2: Transformer equivalent circuit with no leakage flux and optimum load.

In order to analyze the circuit, a first assumption is made by considering that the magnetizing current, I_m, is in quadrature with the pure resistive load current, $I_s^{'}$, therefore, the following expression is valid:

$$I_p^2 = I_m^2 + I_s^{'2} \tag{3.6}$$

The magnetizing current can be written in a first step through Ohm's Law and then have the primary voltage term substituted by making use of the transformer voltage ratio (2.15). The inductance term can also be expanded by applying expression (2.32) and subsequently replace the A_c term with the result from relation (3.2). After simplifying terms and rearranging, the magnetizing current is given by:

$$I_m = \frac{V_p}{\omega L_m} = \frac{K_f B_{ac} M_{PL}}{2\pi \mu_0 \mu_r N_p} \tag{3.7}$$

An expression for the load current can then be achieved by solving (3.6) for $i_s^{'}$ and have the magnetizing current term replaced with expression (3.7) to reach the following result:

$$I_s^{'} = \sqrt{\left(I_p^2 - \left(\frac{K_f B_{ac} M_{PL}}{2\pi \mu_0 \mu_r N_p} \right)^2 \right)} \tag{3.8}$$

Its then important to attain an explicit expression for the transformer secondary turns. This can be obtained by starting with the transformer current ratio (2.24), solving for N_s and then

substituting the load current term with expression (3.8). With this manoeuvre, the transformer secondary turns can be computed with:

$$N_s = \frac{N_p}{I_s}\sqrt{I_p^2 - \left(\frac{K_f B_{ac} M_{PL}}{2\pi\mu_0\mu_r N_p}\right)^2} \tag{3.9}$$

The output power delivered to the load is expressed by solving (3.2) for A_c and then multiplying both sides of the equation with i_s to get a term equal to P_o. After simplifying terms and rearranging the equation, the output power is formulated through:

$$P_o = K_f B_{ac} f N_p A_c \sqrt{I_p^2 - \left(\frac{K_f B_{ac} M_{PL}}{2\pi\mu_0\mu_r N_p}\right)^2} \tag{3.10}$$

were it is evident that the output power is lowered by the magnetizing current term. It should also be noted that expression (3.10) is only valid when $I_p^2 > (K_f B_{ac} M_{PL}/2\pi\mu_0\mu_r N_p)^2$.

3.3.2 No leakage flux and variable load

A second, more accurate, approximation on modelling the transformer is to, as before, neglect both the winding resistances as well as the hysteresis and eddy current losses, and assume no leakage flux is present. However, in this case the power supply is accounted for by an variable resistive load in parallel with the secondary winding. By doing so, the transformer voltages and currents will be affected by load variations.

The magnetizing component of the transformer is represented by an inductance, L_m, in parallel with the ideal transformer. It is also assumed that the core is operating sufficiently below saturation, hence core non-linearity effects can also be ignored and L_m is constant. Figure 3.3 represents the equivalent circuit for this case, notice that the resistive load as been reduced to the primary side and is represented accordingly.

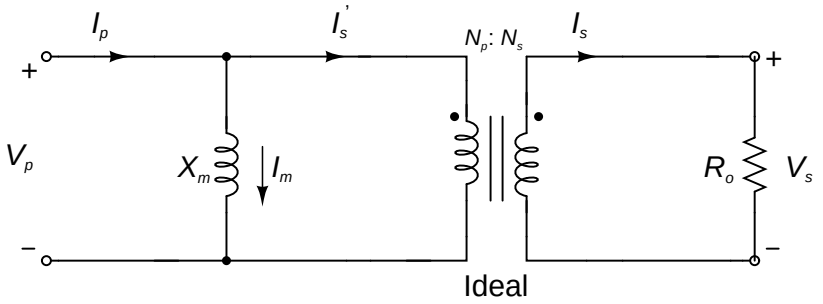

Figure 3.3: Transformer equivalent circuit with no leakage flux and variable load.

The first step to evaluate the circuit of Figure 3.3 is to consider that the magnetizing current, I_m, is in quadrature with the load current, $I_s^{'}$, hence the expression (3.6) is again in use.

It is interesting to study the upper-bound case in which the secondary voltage is maximum and is given by:

$$v_{s_{max}} = \omega N_s B_{ac} A_c/\sqrt{2} \tag{3.11}$$

and thus the magnetizing current will also reach a maximum value denoted with:

$$I_{m_{max}} = \frac{v_{s_{max}} \frac{N_p}{N_s}}{\omega L_m} = \frac{B_{ac} M_{PL}}{\mu_0 \mu_r N_p \sqrt{2}} \tag{3.12}$$

For the general case, the secondary voltage is expressed through Ohm's Law and can be reduced to the primary side by making use of (2.26) as:

$$V_p = R_o \left(\frac{N_p}{N_s}\right)^2 I_s^{'} \tag{3.13}$$

Introducing the result of equation (3.13) in the magnetizing current expression (3.7) leads to the following conclusion after simplifying and rearranging terms:

$$I_m = \frac{R_o I_s^{'} M_{PL}}{\omega \mu_0 \mu_r N_s^2 A_c} \tag{3.14}$$

The load current is written by starting with (3.6) and solving for $i_s^{'}$. Afterwards substituting the magnetizing current term with expression (3.14) enables the load current expression:

$$I_s^{'} = \frac{I_p}{\sqrt{1 + \left(\frac{R_o M_{PL}}{\omega \mu_0 \mu_r N_s^2 A_c}\right)^2}} \tag{3.15}$$

There are two possible expressions for the output power in this case. One starts with the notice that the output power can be written directly in terms of the output resistance and the load current balanced by the square of the transformer ratio. Subsequently, the load current term is replaced with (3.15) and after rearranging terms the output power is dictated by:

$$P_o = \left(\frac{N_p}{N_s}\right)^2 R_o I_s^{'2} = \frac{R_o \left(\frac{N_p}{N_s}\right)^2 I_p^2}{1 + \left(\frac{R_o M_{PL}}{\omega \mu_0 \mu_r N_s^2 A_c}\right)^2} \tag{3.16}$$

Another path is to equate (3.2) for A_c and then multiply both sides of the equation with I_s to get a term equal to P_o. Since the load current I_s can be written as $I_s^{'}$ through the transformer current ratio, it is a matter of substituting it with (3.15) and rearrange the equation to achieve the output power expression:

$$P_o = N_p A_c K_f B_{ac} f \frac{I_p}{\sqrt{1 + \left(\frac{R_o M_{PL}}{\omega \mu_0 \mu_r N_s^2 A_c}\right)^2}} \tag{3.17}$$

An expression for the transformer secondary turns is delivered by picking the transformer current ratio (2.24) and replacing the load current with (3.15) while raising both sides of the equation to the power of two. Afterwards, multiple both sides of the equation with N_s^2 to formulate a bi-quadratic equation. The resultant bi-quadratic equation has the following solution:

$$N_s = \sqrt{\left(\frac{N_p I_p R_o}{\sqrt{2} v_s}\right)^2 \pm \sqrt{\left(\frac{N_p I_p R_o}{\sqrt{2} v_s}\right)^4 - \left(\frac{M_{PL}}{\omega \mu_0 \mu_r N_s^2 A_c}\right)^2}} \tag{3.18}$$

3.3.3 With leakage flux and variable load

Finally, a more accurate approximation of modelling the transformer is to, as before, neglect both the winding resistances as well as the hysteresis and eddy current losses and consider leakage fluxes, while representing the RIOL power supply with an variable resistive load.

In addition, leakage flux is assumed present but it is lumped and reduced to the primary side of the transformer, being accounted for with an inductance, $L_s^{'}$. This assumption is valid since in this case most of the leakage flux is situated in the secondary side of the transformer.

The magnetizing component of the transformer continues to be represented by an inductance, L_m, in parallel with the ideal transformer. It is also assumed that the core is operating sufficiently below saturation, hence core non-linearity effects can also be ignored and L_m is constant.

Figure 3.4 shows the equivalent circuit for this case, notice that all components have been reduced to the primary side and are represented accordingly.

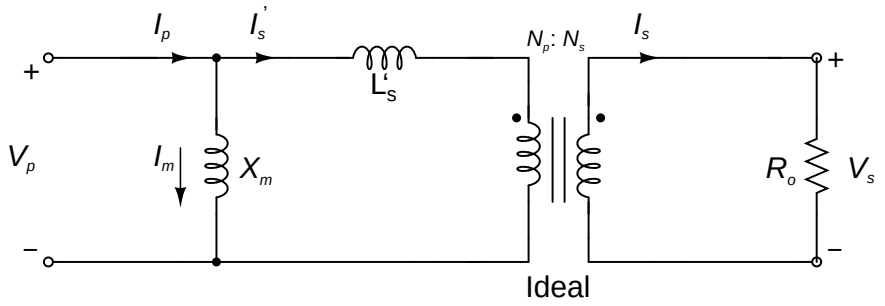

Figure 3.4: Transformer equivalent circuit with leakage flux and variable load.

In order to assess the circuit of Figure 3.4, the load current $i_s^{'}$ can be written using the current divider formula, where $R_o^{'} = R_o \left(\frac{N_p}{N_s}\right)^2$, as:

$$\bar{I_s^{'}} = \frac{\jmath\omega L_m}{R_o^{'} + \jmath\omega(L_m + L_s^{'})}\bar{I_p} \tag{3.19}$$

Under the assumption that the magnetizing current is in quadrature with the primary current, expression (3.6) is valid and therefore the load current is found by considering only the complex modulus of relation (3.19):

$$I_s^{'} = \frac{I_p}{\sqrt{\left(1 + \frac{L_s^{'}}{L_m}\right)^2 + \left(\frac{R_o M_{PL}}{\omega\mu_0\mu_r N_s^2 A_c}\right)^2}} \tag{3.20}$$

The output power is obtained by introducing the load current expression (3.20) in the relation:

$$P_o = R_o \left(\frac{N_p}{N_s}\right)^2 I_s^{'2} = \frac{R_o \left(\frac{N_p}{N_s}\right)^2 I_p^2}{\left(1 + \frac{L_s^{'}}{L_m}\right)^2 + \left(\frac{R_o M_{PL}}{\omega\mu_0\mu_r N_s^2 A_c}\right)^2} \tag{3.21}$$

where it can be deduced that for higher values of the load resistance, R_o, the term related to the leakage flux looses importance.

3.4 Design procedure

A transformer is frequently the heaviest and bulkiest item in the power supply. It also has a significant effect upon the overall performance and efficiency of the system. Accordingly, the design of such transformer has an important influence on the overall system weight, power conversion efficiency and cost. A series of tradeoffs are necessary to achieve design optimization because of the interdependence and interaction of parameters. It is not possible to optimize all parameters in a single design because of their interaction and interdependence [9].

In the design procedure of a transformer suited for the RIOL it is customary to adopt one of the approximate forms of the equivalent circuit of Figure 2.5 described in Section 3.3. The approximations chosen in a particular case depend largely on physical reasoning based on orders of magnitude of the neglected quantities.

The initial step is to designate the inputs to the procedure as the design is faced with a set of constrains that must be observed. These will be a direct consequence of the specifications enumerated in Section 3.1 and start by picking the variables to consider as inputs. For the RIOL transformer the inputs and assumptions are as follow:

- Selection of proper core material since each material has its own optimum point in the cost, size, frequency and efficiency spectrum. In this case, as discussed in Section 3.2, the optimum choice lies in silicon steel laminations with a thickness of $0,35$ mm.
- The primary current is dictated by the transmission line as a sinusoidal current with a frequency of $f = 50$ Hz and an amplitude range of $I_p = [100; 1000]$ A;
- Current density in the secondary is assumed equal to the transmission line value, therefore $J = 200$ A/cm^2;
- The cylindrical core shape, as seen in Figure 3.5, is generally seen as the best possible since the current flowing in the power cable produces flux lines which are tangencial to circular paths around the cable. The core will be comprised of two halves as a result of the separable core needed for clamp-on.
- Since M_{PL} of the core is a critical design parameter, the length of the core, l_c will be made much longer than the radius. This is set because the core cross-sectional area, A_c, of a cylindrical object varies linearly with the length. Therefore, it is possible to obtain a lower weight transformer even knowing the fact that the weight of the secondary windings will increase as the length of the core is made longer.
- The core's window area, W_a must be set to comprise the power cable, plus the secondary windings and an additional minimum space to allow the mechanical clearance and cable deflection under sag conditions, represented by 1 cm. Thus, the inner diameter, ID, must

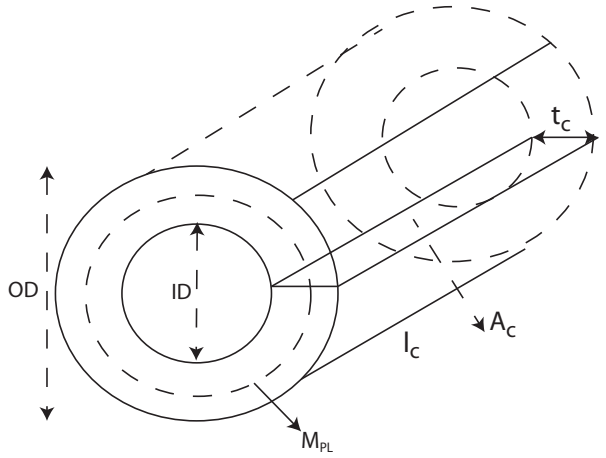

Figure 3.5: Transformer cylinder core outline.

be set as a predefined minimum. The geometric relations that are associated to a cylindrical core as shown in Figure 3.5 are:

$$ID = 2\sqrt{A_{wp}/\pi} + 1/100 \tag{3.22}$$

$$W_a = \pi(ID/2)^2 \tag{3.23}$$

$$t_c = A_c/l_c \tag{3.24}$$

$$OD = ID + 2t_c \tag{3.25}$$

$$M_{PL} = \pi(OD - t_c/2) \tag{3.26}$$

$$MLT = 2l_c + \pi t_c \tag{3.27}$$

$$A_t = 2\pi(OD/2)(OD/2 + l_c) \tag{3.28}$$

$$c_v = A_c M_{PL} \tag{3.29}$$

$$W_{tfe} = c_v \gamma 10^3 \tag{3.30}$$

$$W_{tcu} = \gamma_{cu} N_s A_{ws} MLT \tag{3.31}$$

- A temperature rise of less than $30\ ^oC$ should be observed in the transformer core in order to maintain safety of the equipment. The dissipated power per surface area of the core, Γ, and the matching temperature rise, T_r, can be computed through [9]:

$$\Gamma = P_\Sigma / A_t \tag{3.32}$$

$$T_r = 450 \cdot \Gamma^{(0,826)} \tag{3.33}$$

- Magnetic flux density should be as high as possible, only limited by the characteristics of the material. For silicon steel the maximum value before entering in the saturation zone is approximately $B_{ac} = 1,6$ T, so the magnetic flux density will vary from remanence to $1,6$ T.

- Lastly, because the RIOL is supplied at $V_{DC} = 55$ V and given the power rectifier working scheme designed in [14], the secondary voltage must comply with [7]:

$$V_s = \frac{\pi V_{DC}}{2\sqrt{2}} \tag{3.34}$$

With these inputs enabled as a starting point, there is a need to choose one of the models in Section 3.3 to complete the set of equations needed to estimate the transformer parameters and performance. After picking the desired model, the design process can be computed by varying a set of parameters comprised of the load resistance, R_o, the input current I_p, the length of the core l_c, the core cross sectional area A_c and the magnetic flux density B_{ac}.

The process is started by reading the values for the constants: $f = 50$ Hz, $K_f = 2\pi/\sqrt{2}$, $N_p = 1$ because the primary winding is the transmission line cable, $J = 200$ A/m^2 since it is assumed equal to the power line, $A_{wp} = 500$ mm^2 that is the diameter of the cable, $V_{DC} = 55$ V which is the voltage in which the RIOL is supplied. Afterwards the core material is selected from Table 3.2 and the corresponding core loss coefficients are taken from Table 3.3.

The model of sub-section 3.3.2 is chosen in order to have the design equations. The process is analogous for the other models of section 3.3. By imposing the initial values for the variables R_o, I_p, l_c, A_c and B_{ac}, the first step can be taken in computing the remaining variables:

1. Compute the geometric parameters of the core with relations (3.22)-(3.28);
2. Establish V_s resorting to (3.34);
3. Obtain the number of turns of the secondary winding, N_s, by using expression (3.18);
4. Calculate the load current, $I_s^{'}$,that is drawn by the RIOL with equation (3.15);
5. Compute the magnetizing inductance, L_m, from (2.31);
6. With the previous result, determine the magnetizing current, I_m given by (3.14);
7. Determine the secondary current, I_s, directly from the transformer ratio of (2.24);
8. Receive the values for the winding resistances, R_p and R_s, from (2.20);
9. Equate the total copper losses, P_{cu}, using (2.40) and the values previously acquired;
10. Measure the secondary winding copper weight, W_{tcu}, with equation (3.31);
11. Gauge the volume of the transformer core, c_v, by employing relation (3.29);
12. Calculate the core weight, W_{tfe}, with (3.30) and the corresponding density from Table 3.1;
13. Estimate the watt-per-kilogram loss, [W/kg], that occurs in the core by applying equation (3.1) with the associated coefficients denoted in Table 3.3;

14. Compute the total core loss, P_{fe}, from expression (2.42);
15. Sum the copper losses, P_{cu}, with the core losses, P_{fe} to achieve the total power loss P_{Σ};
16. Assess the output power, P_o delivered to the load by executing expression (3.17);
17. Determine the transformer efficiency, η, directly from relation (2.39);
18. Compute the transformer total weight, W_t, by summing the secondary winding copper weight, W_{tcu}, and the core weight, W_{tfe};
19. Estimate the dissipated power per surface area, Γ, through relation (3.32);
20. Receive the temperature rise above ambient temperature, T_r, from equation (3.33);
21. Assign the next set of values for variables R_o, I_p, l_c, A_c, B_{ac} and return to step 1 to repeat computation. This is done until ending the sweep through the desired range of values.

A series of theoretical can be drawn through the variation of the degrees of freedom that were established by the changing input variables R_o, I_p, l_c, A_c and B_{ac}.

A simulation is performed by starting with the variation of the output resistance, R_o, while the input current, I_p, is settled at 300 A, the magnetic flux density of operation is $B_{ac} = 1,6$ T and the core has a cross-section of $A_c = 50$ cm^2 with a length of $l_c = 30$ cm. The chosen material for this simulation is silicon steel with a thickness of $0,35$ mm. Table 3.4 sums up the values attributed to the variables of interest for this simulation case.

Table 3.4: Values for simulation of the output resistance variation

I_p $[A]$	B_{ac} [T]	A_c [cm^2]	l_c [cm]	Thickness [mm]	R_o $[\Omega]$
300	1,6	50	30	0,35	[0;5]

Figure 3.6(a) shows the effect of varying R_o on the output power delivered to the load, P_o. In the same manner, Figure 3.6(b) denotes the impact that a change in R_o has on the magnetizing current, I_m.

By inspecting Figure 3.6(a) it can be seen that the output power faces a considerable gap for values of the output resistance lower than $1\ \Omega$. This effect then fades away for values above $1\ \Omega$ and the output power stabilizes around 525 W with a tendency to slowly rise as the value for the output resistance increases. This behaviour can be explained by looking to expressions (3.18) and (3.17) and realizing that the number of secondary turns, N_s, will slowly adapt to the rise of the output resistance and thus compensate its effect on the output power.

A study of Figure 3.6(b) further corroborates the above mentioned point since the magnetizing current, I_m, is significantly high for values lower than $1\ \Omega$, thus diminishing the load current component and drastically lowering the output power. As the output resistance increases, the

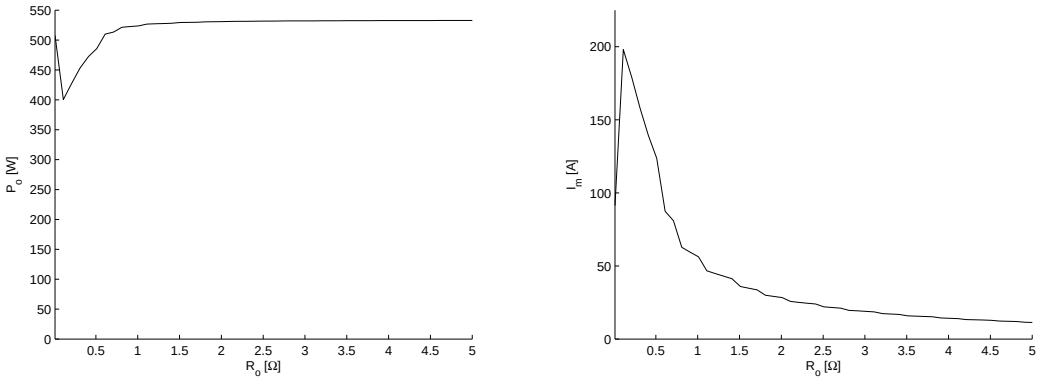

(a) Output power. (b) Magnetizing current.

Figure 3.6: Effect of varying the output resistance.

secondary turns also increase and have a quadratic ratio in the magnetizing current expression (3.14). Hence, in this case the magnetizing current lowers and decays into a value of around 20 A, were it stabilizes. In other words, the magnetizing current significantly loses influence in the output power as the output resistance increases.

Another simulation is performed by varying the length of the transformer core, l_c. Table 3.5 sums up the values attributed to the variables of interest for this simulation case.

Table 3.5: Values for simulation of the transformer length variation

I_p $[A]$	B_{ac} [T]	A_c [cm^2]	l_c [cm]	Thickness [mm]	R_o $[\Omega]$
300	1,6	50	[10;100]	0,35	2

Two results of this simulation are indicated in Figures 3.7(a) and 3.7(b). The first reveals the relation between the transformer core length and the copper, core and total losses. The second evidences the behaviour of the weight of the secondary winding and the core as well as their aggregate under a change in the transformer core length.

Through examination of Figure 3.7(a), the total loss denotes a minimum value when the copper and core losses are equalled. This occurs for a transformer length of around 15 cm, from which point the total losses rise sharply under the influence of the enlarged copper losses as the transformer core length increases. The conclusion is explained by the relation of l_c and *MLT* in (3.27) and the impact it has on the secondary winding resistance (2.20) that is used to compute copper losses through (2.40). Observing Figure 3.7(b) reveals that the transformer core weights less as the length increases for the same cross section. On the other hand as the length of the secondary winding increases so does its weight, but it has little impact on the total transformer weight since the net result is balanced by the decrease of weight in the core. Hence, incrementing the transformer core length for the same cross-section does reduce weight, to a certain point, but caution should be taken since it also increases copper losses significantly.

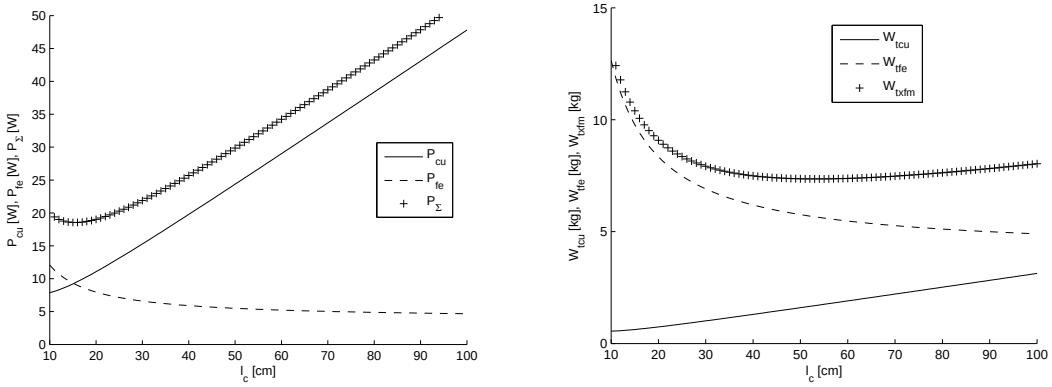

(a) Copper loss, core loss and total loss.

(b) Secondary winding weight, core weight and total weight.

Figure 3.7: Effect of varying the transformer core length.

Another interesting simulation is to observe the alterations associated with the change in the magnetic flux density of operation, B_{ac}. Table 3.6 sums up the values attributed to the variables of interest for this simulation case.

Table 3.6: Values for simulation of the magnetic flux density variation

I_p $[A]$	B_{ac} [T]	A_c [cm^2]	l_c [cm]	Thickness [mm]	R_o $[\Omega]$
300	[0;1,8]	50	30	0,35	2

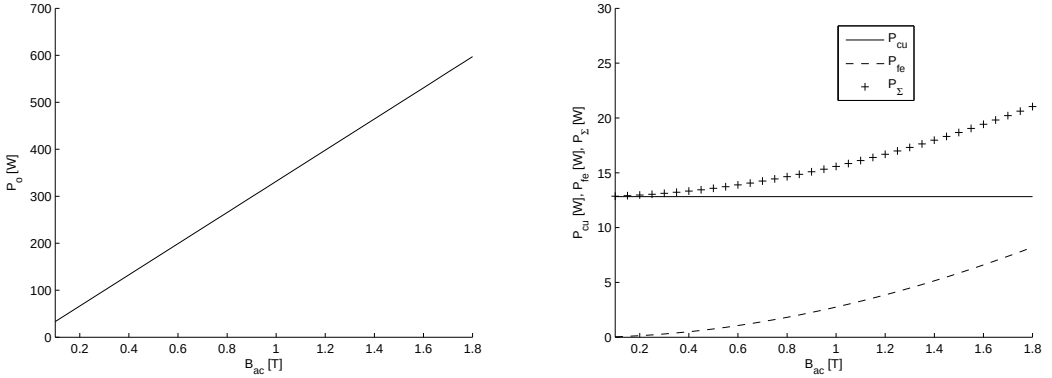

(a) Output power.

(b) Copper loss, core loss and total loss.

Figure 3.8: Effect of varying the magnetic flux density of operation.

Figure 3.8(a) reflects the consequence of varying the magnetic flux density of operation on the output power. The relationship between P_o and B_{ac} is quasi-linear and it is evident that B_{ac} has a significant role in the magnitude of the output power. The higher the magnetic flux density, the higher output power, therefore, the usage of a material that can be operated at a high magnetic flux density is very important to the performance of the transformer.

The repercussions of varying the magnetic flux density on the copper losses, core losses and total losses are illustrated in Figure 3.8(b). As expected it has no effect on the copper losses and thus these remain constant over the range of values for B_{ac}. However, core losses depend directly of the magnetic flux density as seen in expression 3.1 and is shown in 3.8(b), but the magnitude of increased losses is less significant when compared to the rise in output power as the magnetic flux density is incremented.

Its also important to simulate the changes dictated by the variation of the effective cross section of the core, A_c. Table 3.7 gathers the values attributed to the variables of interest for this simulation case. The results in the form of the output power and the magnetizing current, subjected to a varying cross section of the core, can be found in Figures 3.9(a) and 3.9(b), respectively.

Table 3.7: Values for simulation of the core cross-section variation

I_p $[A]$	B_{ac} [T]	A_c [cm^2]	l_c [cm]	Thickness [mm]	R_o $[\Omega]$
300	1,6	[10;100]	30	0,35	2

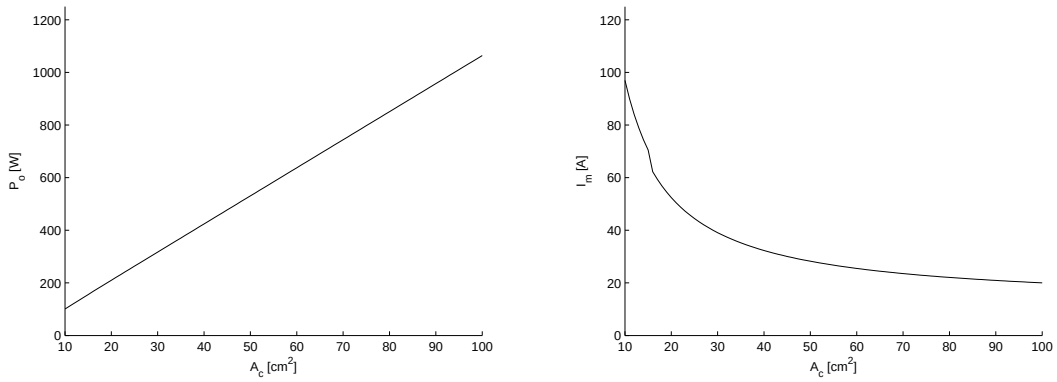

(a) Output power.

(b) Magnetizing current.

Figure 3.9: Effect of varying the effective cross section of the core.

After inspecting Figure 3.9(a), it can be stated that the output power of the transformer has a quasi-linear relationship with the effective cross section of the core. Similarly with the magnetic flux density, the larger the cross section, the higher the output. Of course, the obvious drawback is the drastic increase in core volume that a larger cross section dictates as shown in expression (3.29) and thus an increased core weight through (3.30).

The magnetizing current is also significantly dependent of the core cross section as observed in Figure 3.9(b). For a cross section below 30 cm^2, the magnetizing current reaches relatively high magnitudes that impair the load current and thus the output power as corroborated in Figure 3.9(a). Above the referred value, the magnetizing current fades away, noticeably decreasing in magnitude, and starts to stabilize past the 60 cm^2 mark as the influence of the core cross section begins to dominate the magnetizing current expression seen in (3.14).

Its also possible to estimate the importance of varying the grade of the silicon steel used in the core. For this effect, a simulation is performed with a fixed transformer length of $l_c = 30$ cm, an output resistance of $R_o = 2\ \Omega$ and an cross section of A_c = 50 cm^2. The grades of silicon steel are established by Tables 3.2 and 3.3. The input current is varied and the output power for the different grades is shown in Figure 3.10(a). Afterwards, the magnetic flux density is varied and the core loss for the different grades is presented in Figure 3.10(b).

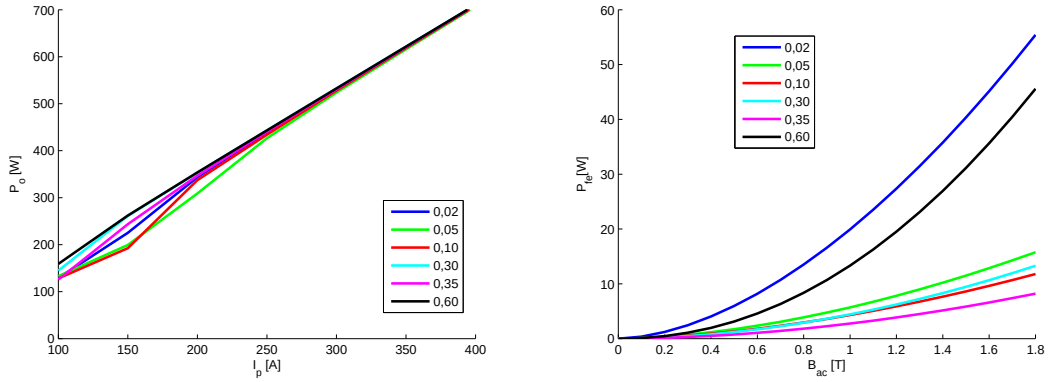

(a) Output power.

(b) Core losses.

Figure 3.10: Effect of varying the input current and the grade of silicon steel.

Figure 3.10(a) demonstrates that the grade of the silicon steel used is not relevant when the input current is past 300 A since the differences between them are negligible. For values below 250 A there are minor differences with the thicker laminations providing more output power than their thinner counterparts.

As for Figure 3.10(b), the thinner and the thickest laminations presents the higher core loss of the group and therefore are not ideal for the transformer core. It should be noted that the lamination with $0,35$ mm presents the lowest core loss throughout the range of values for the magnetic flux density and is the most cost effective lamination for the transformer core.

4

Transformer description

The transformers used throughout this thesis are described in this chapter. Each transformer is presented in detail and key specifications are discussed. Physical and electrical specifications are enumerated for each individual transformer.

Firstly, the core dimensions and physical characteristics are given and compared between each other. Subsequently, the magnetic properties inherent of the materials utilized in each core are studied and measurements are taken to evaluate key features such as the magnetic permeability of the materials that constitute the core.

Afterwards, the important open circuit and short circuit tests are performed to each of the transformers and the results are explained and related to the models in Chapters 2 and 3.

Measurements are performed to estimate parameters of the transformer model, namely the magnetizing inductance and resistance, the total leakage flux referred to the primary side, the winding inductances and resistances and the total copper loss.

4.1 Short UI transformer

The first transformer to be described was constructed during the course of the work developed in [7]. Figure 4.1 shows the front view and the side view of the short UI transformer. It has been designed and assembled to comply with the power needs of the RIOL (1 kW), disregarding the effect of the magnetizing current.

This transformer is built with UI shaped silicon steel laminations. The core is stacked in a non-interleaved fashion, which originates a significant air-gap that hinders efficiency of the transformer. Each iron lamination has a thin coating of insulation on each face. This coating thereby insulates each lamination from the other minimizing eddy currents circulating in the core.

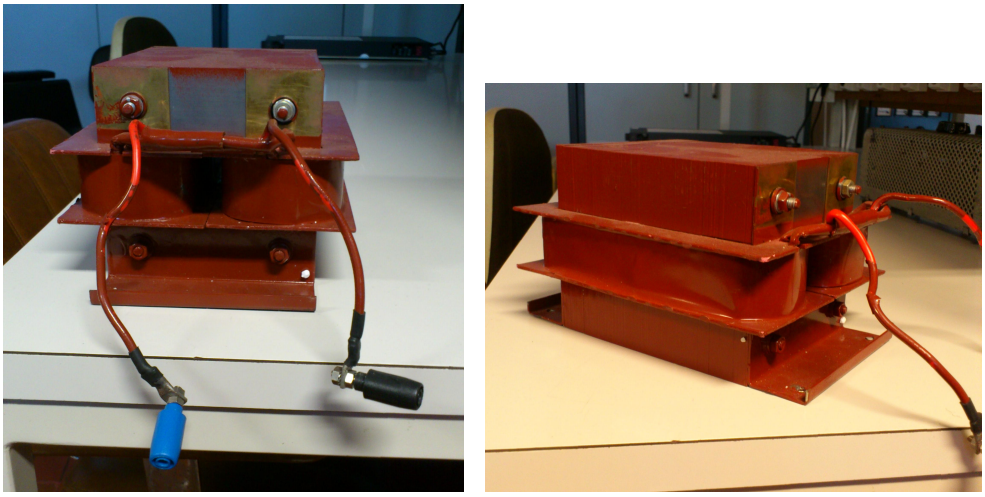

Figure 4.1: Front and side view of short UI transformer.

The relevant physical properties of the transformer in question are denoted in Table 4.1. In itself the transformer is bulky, as denounced by the total weight and core volume. Notice the significantly high M_{PL} in comparison with the *MLT* which, referring to expression (3.14), suggests a high magnetizing current being developed in the core. Thus, it is expected that the output power will be significantly reduced by this particular physical feature.

Table 4.1: Physical properties of the short UI transformer

A_c [cm^2]	W_a [cm^2]	t_c [cm]	l_c [cm]	M_{PL} [cm]	*MLT* [cm]	W_t [kg]	c_v [dm^3]
60,0	16,0	4,0	15,0	32,0	38,0	16,2	1,9

The secondary winding of the transformer is comprised of 20 turns of a 2 mm copper conductor with insulation. The total weight of the secondary is around 400 g, thus being a small part of the transformer total weight.

4.1.1 Magnetic permeability test

An experimental test was performed in order to measure the magnetic permeability of the material that composes the core. This test consisted of connecting in parallel a RC low pass integrator probe to the secondary of the transformer and carry out measurements of the capacitor voltage, the primary and secondary currents as well as the primary and secondary voltages after injecting a primary current into the transformer.

The result of integrating the secondary voltage, as expressed by Faraday's law (2.14), is the time variant flux ϕ. By making use of this result and the transformer core cross-section, it is possible to compute the magnetic flux density, B, through (2.9). On the other hand, calculating the magnetic field, H, is achievable by employing expression (2.10) with the measurement of the primary current.

With the magnetic flux density and the magnetic field acquired, the $B - H$ loop is drawn for the material that composes the transformer core. It is then feasible to compute various magnetic permeabilities through this hysteresis loop since the magnetic permeability, μ, is the slope at a given place in the loop. The maximum value for the magnetic permeability is located below saturation, as shown in Figure 2.3(b), and is typically the standard for evaluating the performance of a magnetic material.

The $B - H$ loop that was attained through this experimental procedure for the short UI transformer is shown in Figure 4.2. At a first glance it is evident that core loss is significantly high since the area contained by the hysteresis loop is also quite considerable, indicating a rather inefficient transformer.

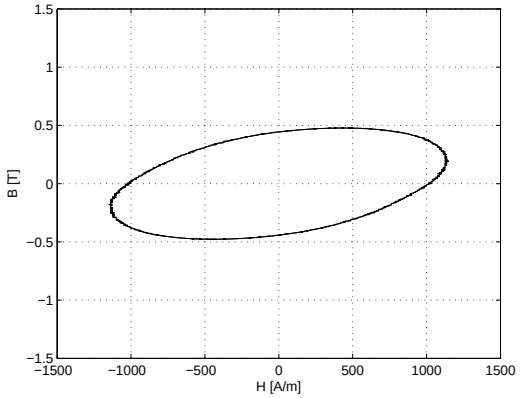

Figure 4.2: B-H loop for short UI core.

Further investigating Figure 4.2 also reveals that the core supports a much lower maximum flux density, $B_{max} \approx 0,48$ T, than it is typical for silicon steel cores. Adding to that fact, the remanence flux density is $B_r \approx 0,44$ T, which is marginally close to the maximum. Thus, the coercivity that is required to remove the polarized flux remaining in the core is also significantly high, with a value of $H_c \approx 1038$ A/m.

The maximum relative magnetic permeability that is obtained from the derivative taken below saturation in the $B - H$ loop of Figure 4.2 is $\mu_{r_{max}} = 1032$. This value indicates the negative influence of the air-gap that is established in the core due to the non-interleaved laminations.

4.1.2 Open circuit and short circuit tests

The open circuit test is executed by keeping the secondary open circuited and applying voltage to the primary. Typically, the voltage applied is the rated voltage, but because of the principle of operation that characterizes a current transformer, the voltage is kept at a value that puts the transformer on the edge of saturation.

The result of the open circuit test is shown in Figure 4.3. The measured *rms* magnitude for the secondary open circuit voltage is $V_{oc} = 19,72$ V and for the primary open circuit current is $I_{oc} = 152$ A. The measured value for the open circuit power was $P_{oc} = 80,26$ W.

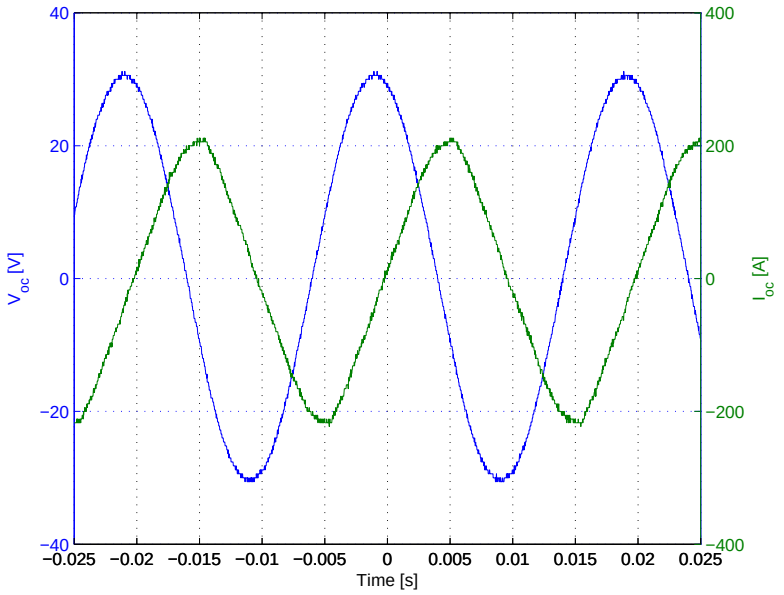

Figure 4.3: Secondary open circuit voltage (blue) and primary current (green) for the short UI transformer.

An open circuit impedance, referred to the primary side of the transformer, can be established by looking into the primary and associating the impedance of the primary circuit with the impedance of the exciting branch.

Typically, the impedance of the exciting branch is relatively large, hence the voltage drop in the primary impedance caused by the exciting current is usually negligible. In this case the primary impressed voltage nearly equals the *emf* induced by the resultant core flux. Under these assumptions the open circuit impedance, Z_{oc}, is:

$$\bar{Z}_{oc} = R_p + \jmath X_p + Z_\phi \approx \frac{R_c(\jmath X_m)}{R_c + \jmath X_m} \tag{4.1}$$

With the measurements taken and neglecting the primary leakage impedance for an open circuit impedance given by 4.1, the magnetizing resistance and reactance can be computed as:

$$R_c = \frac{V_{oc}^2}{P_{oc}} = 4,85\ \Omega \tag{4.2}$$

$$Z_\phi = \frac{V_{oc}}{I_{oc}} = 129,7\ \text{m}\Omega \tag{4.3}$$

$$X_m = \frac{1}{\sqrt{(1/Z_\phi)^2 - (1/R_c)^2}} = 129,8\ \text{m}\Omega \rightarrow L_m = 413,11\ \mu\text{H} \tag{4.4}$$

were L_m can be utilized, through 2.32, to calculate an approximation of the relative magnetic permeability of this transformer core as $\mu_r \approx 877$. The computed value is relatively consistent with the maximum value for the magnetic permeability that was obtained in sub-Section 4.1.1.

The magnetizing resistance can be used to approximate core loss in the transformer, in which case these are equal to the open circuit power and are linked as follow:

$$P_{fe} = P_{oc} = V_{oc}^2/R_c = 80,26\ \text{W} \tag{4.5}$$

The short circuit test is executed by applying a voltage to the primary side and short circuit the secondary terminals with a conductor of very small length and impedance. The imposed voltage is maintained at around 10% to 15% of rated voltage in order to reach the rated current. The result of the short circuit test is registered in Figure 4.4.

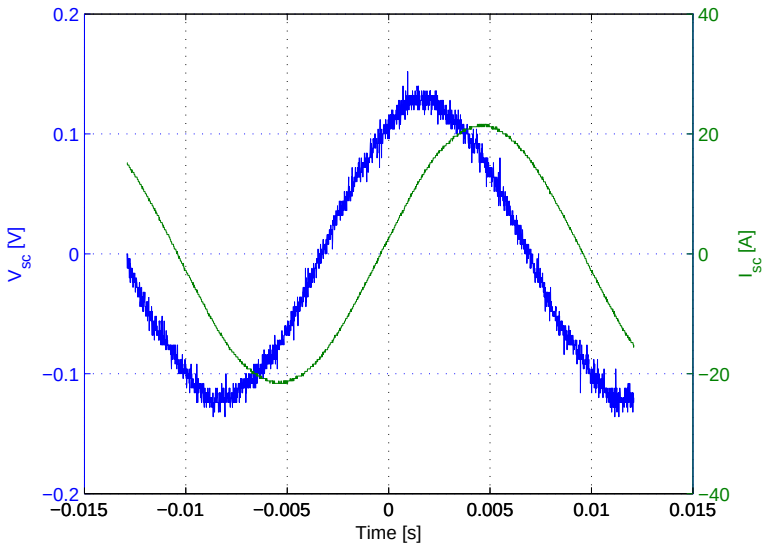

Figure 4.4: Primary short circuit voltage (blue) and secondary current (green) for the short UI transformer.

The measured *rms* magnitudes for the short circuit voltage is $V_{sc} = 0,084$ V and for the short circuit current is $I_{sc} = 15,12$ A. In this case the measured short circuit power is $P_{sc} = 25,2$ W.

In this case, the short circuit impedance can be seen as the series of the primary winding impedance with the parallel of the magnetizing branch with the secondary winding impedance. On the other hand, since the magnetizing branch is typically larger than the secondary leakage

impedance, a small portion of current will flow to the magnetizing branch. Hence, the short circuit impedance, Z_{sc}, can be approximated as:

$$\bar{Z}_{sc} = R_p + \jmath X_p + R_s + \jmath X_s = R_{sc} + \jmath X_{sc} \tag{4.6}$$

The short circuit impedance, comprised of the resistance and reactance, is then computed by resorting to the measurements of the short circuit voltage and current as well as the short circuit power. For this case, with the values all referred to the primary side, the relations are:

$$Z_{sc} = \frac{V_{sc}}{I_{sc}} = 5,6 \text{ m}\Omega \tag{4.7}$$

$$R_{sc} = \frac{P_{sc}}{I_{sc}^2} = 110,2 \text{ m}\Omega \tag{4.8}$$

$$X_{sc} = \sqrt{Z_{sc}^2 - R_{sc}^2} = 110,1 \text{ m}\Omega \rightarrow \frac{X_{sc}}{\omega} = L_m || L_{l_s}^{'} = 350,42 \ \mu\text{H} \tag{4.9}$$

As stated in expression 4.9, the short circuit reactance corresponds to the parallel of the magnetizing inductance with the secondary winding leakage inductance. Therefore, it is possible to compute a total leakage flux coefficient that is referred to the primary winding. This coefficient lumps all of the leakage flux that is primarily associated to the secondary winding and is expressed as:

$$L_s^{'} = -\frac{(L_m || L_{l_s}^{'}) \cdot L_m}{(L_m || L_{l_s}^{'}) - L_m} = 2,3 \text{ mH} \tag{4.10}$$

The short circuit resistance can be interpreted as an equivalent resistance that sums up the primary and secondary winding resistances. In this case, the short circuit resistance is linked to the total copper losses of the transformer. Hence, the short circuit power is also used to estimate the total copper loss and can be related as:

$$P_{cu} = P_{sc} = R_{sc} I_{sc}^2 = 25,2 \text{ W} \tag{4.11}$$

which coupled with the core loss computed in (4.5) amount for a total loss of $P_\Sigma = 105,46$ W. This value signifies the inefficiency of the transformer as a whole and will be evident during the load tests described in Chapter 5.

4.2 Long UI transformer

The second transformer to be described was also developed in the work that was carried out in [7]. Figure 4.5 shows the front view and the side view of the long UI transformer. This transformer was designed with the goal of providing a power of around 1 kW in a situation were the transmission line current is deemed as a mean value in the range of its operation. Other considerations were also taken into account such as diminishing the volume and weight of the core to better follow the specifications that are enunciated in Section 3.1.

As with the first transformer of Section 4.1, UI shaped silicon steel laminations are utilized to form the core stack. The core is stacked in an interleaved fashion, where each lamination is staggered opposite to the other (turned 180^o opposite the other). This provides for the least amount of air gap in the core and the highest possible efficiency. The laminations are also coated with a thin insulation layer that mitigates eddy currents which otherwise would reach a substantial value in the core. This keeps much of the eddy currents contained in a lamination and surpasses circulation of inter-lamination eddy currents.

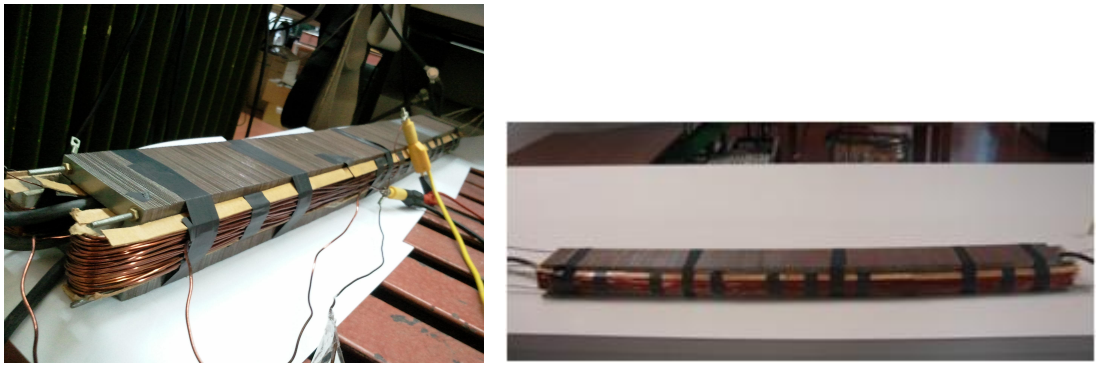

Figure 4.5: Front and side view of long UI transformer.

The important physical properties of this transformer are evidenced in Table 4.2. Through inspection it can be said that this transformer features a higher core cross section in relation to the transformer of Table 4.1, despite being less bulky with a lower weight and volume. This was achieved by lowering the core thickness, t_c, and raising the core length l_c.

Table 4.2: Physical properties of the long UI transformer

A_c [cm^2]	W_a [cm^2]	t_c [cm]	l_c [cm]	M_{PL} [cm]	*MLT* [cm]	W_t [kg]	c_v dm^3]
77,3	12,0	1,0	77,3	18,0	156,6	11,5	1,4

As a result, the M_{PL} is significantly lower, which, coupled with a higher A_c, diminishes the magnetizing current and increments the output power of the transformer as expressed in relations (3.14) and (3.21). On the other hand, notice the substantially high *MLT*, that on its own will mean higher copper losses as seen in Figure 3.7(a).

The secondary winding of the transformer is composed of 30 turns of a 2 mm copper conductor with isolating insulation. The contribution of the secondary winding to the total transformer weight is relatively small, since the secondary weighs around $1,3$ kg, thus being about 11%. In comparison with the short UI transformer, the secondary winding is more relevant to the copper losses due to the higher number of turns and the aforementioned value for the *MLT*.

4.2.1 Magnetic permeability test

In order to assess the magnetic permeability of the core that composes the long UI transformer, a similar test to that of sub-Section 4.1.1 was carried out.

The RC low pass integrator was connected to the secondary winding terminals and measurements of the capacitor voltage, that relates to time varying flux, were taken in conjunction with the primary current that relates to magnetic field. The primary and secondary voltage as well as the secondary current were also registered.

Upon acquiring the magnetic flux density, B, and the magnetic field, H, the $B-H$ loop is drawn for the material in which the core is built. Figure 4.6 is the hysteresis loop for this transformer core, notice that it quite resembles the typical $B-H$ loop for silicon steel as shown in Figure 3.1(a).

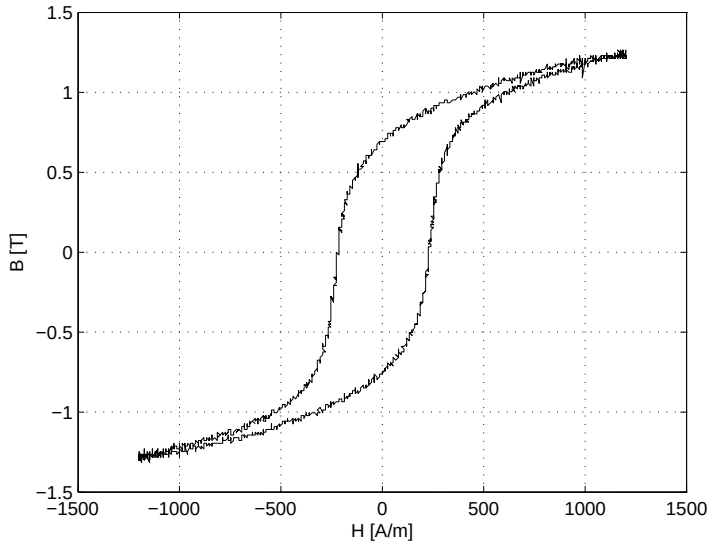

Figure 4.6: B-H loop for long UI core.

As opposed to the hysteresis cycle of Figure 4.2, the cycle of Figure 4.6 has a much smaller area contained inside it, being narrower and closely hugging the initial curve, which suggests a substantially lower core loss and thus higher transformer efficiency.

The long UI transformer also features a material that has a remanence flux density of approximately $B_r \approx 0,69$ T and a coercivity of $H_c \approx 227$ A/m, that denote a *soft* magnetic material suitable for devices which develop alternating fields.

In another important parameter, it can be seen from the hysteresis loop of Figure 4.6 that the maximum magnetic flux density of the material is $B_{max} \approx 1,27$ T. This enables an operation with a higher magnetic flux density than that of the short UI transformer as stated in sub-Section 4.1.1. Hence output power will also be higher since there is a strong relation between magnetic flux density of operation and output power as seen in Figure 3.8(a).

The $B-H$ loop of Figure 4.6 also enables the possibility to estimate the magnetic permeability of the material in question. In order to retrieve the maximum value the slope is calculated in a region well below saturation. The maximum relative magnetic permeability that is computed through this method is $\mu_{r_{max}} = 2067$.

Albeit this value is relatively higher, being approximately double of the one estimated for the short UI transformer, it suggests that the material in which the core is built is of a medium grade cold rolled non-oriented silicon steel as referenced in Table 3.2. With this value of magnetic permeability it is expected that the output power will also be affected favourably as denoted in expression (3.21), since the magnetizing current term will be decreased.

4.2.2 Open circuit and short circuit tests

The open circuit test is carried out in the same manner as described in sub-Section 4.1.2. Figure 4.7 contains the result of the open circuit procedure. As can be observed, the transformer is saturated and this invalidates the calculation of parameters and losses. Unfortunately this test could not be performed again since the transformer has since been disassembled.

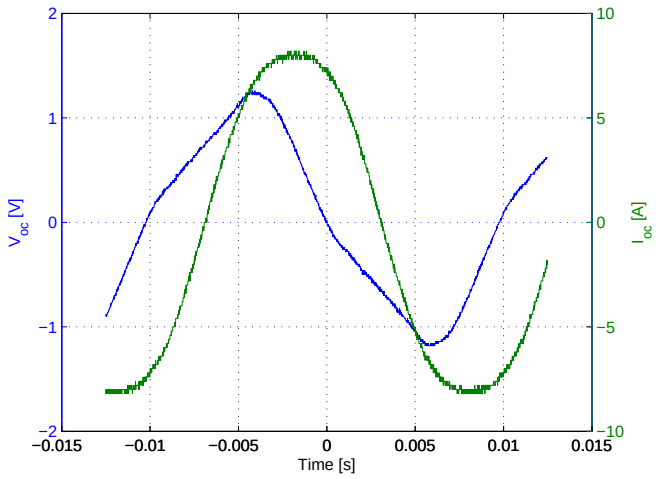

Figure 4.7: Open circuit voltage (blue) and current (green) for the long UI transformer.

As a solution in order to continue the procedure of calculating the open circuit parameters, data of measurements taken from [7] are used in this case. The *rms* magnitudes for the open circuit voltage and current are, respectively, $V_{oc} = 377,1$ mV and $I_{oc} = 5,1$ A, with the measured open circuit power delivered as $P_{oc} = 2,09$ W.

Under the same assumptions that lead to expression 4.1 and resorting to the measurements taken above, the magnetizing resistance and reactance are given directly by:

$$R_c = \frac{V_{oc}^2}{P_{oc}} = 96,1 \text{ m}\Omega \tag{4.12}$$

$$Z_\phi = \frac{V_{oc}}{I_{oc}} = 74,8 \text{ m}\Omega \tag{4.13}$$

$$X_m = \frac{1}{\sqrt{(1/Z_\phi)^2 - (1/R_c)^2}} = 110,0\ m\Omega \rightarrow L_m = 379,09\ \mu\text{H} \tag{4.14}$$

With the value computed for L_m in 4.14, there is a corresponding value for the relative magnetic permeability that can be obtained through 2.32. The computed approximation of the relative magnetic permeability of this transformer core is $\mu_r \approx 234$. This value is significantly detached from the maximum relative magnetic permeability that is indicated in sub-Section 4.2.1.

It should be noted that the magnetic permeability value received from the saturated case in Figure 4.7 is $\mu_r \approx 183$. This leads to a conclusion that albeit not saturated, the transformer is very near saturation on the $B - H$ loop of Figure 4.6, which substantially diminishes the value of the derivative and therefore of the magnetic permeability.

Since the magnetizing resistance computed in (4.12) is linked to core loss in the iron core of the transformer, there is a association of core loss with the measured open circuit power. For this case, the corresponding value is designated by:

$$P_{fe} = P_{oc} = V_{oc}^2/R_c = 2,09 \text{ W} \tag{4.15}$$

which is significantly lower than the core loss for the short UI transformer denoted in (4.5). This conclusion is also coherent with the hysteresis loop of this transformer, seen in Figure 4.6, and the hysteresis loop of the short UI transformer that is shown in Figure 4.2.

The short circuit test is carried out in the same manner as described in sub-Section 4.1.2. Figure 4.8 contains the result of the short circuit procedure with the short circuit voltage and current exemplified.

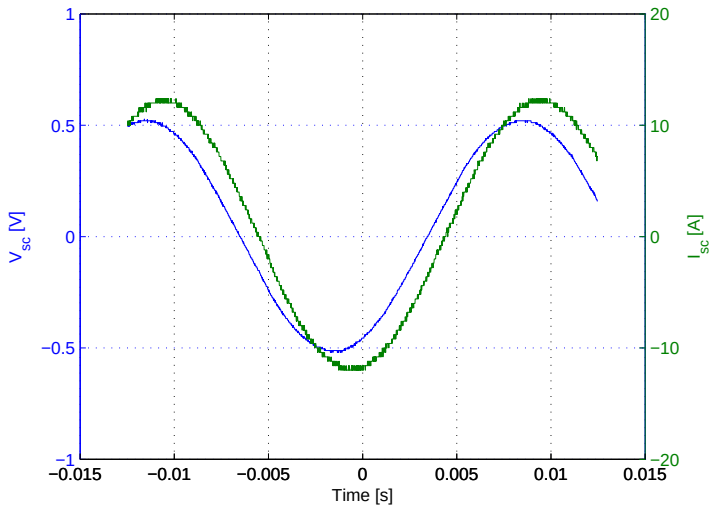

Figure 4.8: Short circuit voltage (blue) and current (green) for the long UI transformer.

The magnitudes for the *rms* short circuit voltage and current are $V_{sc} = 373,4$ mV, $I_{sc} = 8,77$A and the short circuit power for this test was measured at $P_{sc} = 3,23$ W.

With the same assumptions that establish expression (4.6), the short circuit resistance and reactance, that compose the equivalent impedance seen from the primary winding are given by:

$$Z_{sc} = \frac{V_{sc}}{I_{sc}} = 49,3 \text{ m}\Omega \tag{4.16}$$

$$R_{sc} = \frac{P_{sc}}{I_{sc}^2} = 41,9 \text{ m}\Omega \tag{4.17}$$

$$X_{sc} = \sqrt{Z_{sc}^2 - R_{sc}^2} = 7,4 \text{ m}\Omega \rightarrow \frac{X_{sc}}{\omega} = L_m || L_{l_s}^{'} = 23,54 \ \mu\text{H} \tag{4.18}$$

The total leakage flux coefficient that corresponds to all leakage flux in the transformer windings referred to the primary winding is computed using the result given by expression (4.18) and the following relation:

$$L_s^{'} = -\frac{(L_m || L_{l_s}^{'}) \cdot L_m}{(L_m || L_{l_s}^{'}) - L_m} = 25,09 \ \mu\text{H} \tag{4.19}$$

Since the short circuit power can be interpreted as the total copper loss in both transformer windings, the short circuit resistance is also seen as the equivalent resistance to both windings. Therefore, the following expression is valid:

$$P_{cu} = P_{sc} = R_{sc} I_{sc}^2 = 3,23 \text{ W} \tag{4.20}$$

4.3 UU transformer

As with the two previous transformers, the third transformer is also a product of the work performed in [7]. The main design goal was to provide an output power suitable for one third the power needs of the RIOL. That said, it was also important to comply with the specifications presented in Section 3.1, so the total weight, volume and shape of this transformer were tailored to follow the specifications and preliminary considerations.

The construction type is different since this transformer relies on eight UU shaped halves glued together to form the core stack. Each UU half is insulated with a thin layer to diminish the flow of eddy currents between each half of the transformer core. Figure 4.9 shows the front view and the side view of the UU transformer.

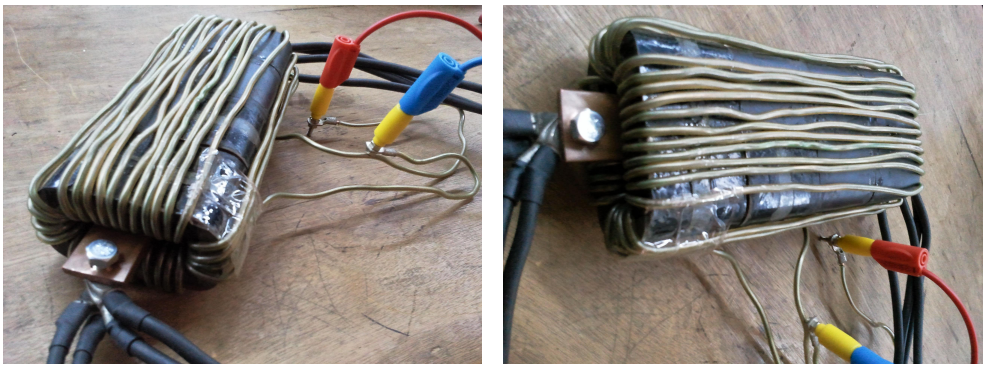

Figure 4.9: Front and side view of UU transformer.

Table 4.3 presents the relevant physical properties that characterize this transformer. Upon first inspection its evident that it his the smallest of the three transformers, both in weight and in volume.

It features a relatively small M_{PL} but on the other hand a substantially low core cross section A_c in comparison with the two previous transformers. These are two crucial parameters in the magnetizing current expression (3.14) and, as such, have an impact on the output of the transformer as seen in Figure 3.9(a).

Table 4.3: Physical properties of the UU transformer

A_c [cm^2]	W_a [cm^2]	t_c [cm]	l_c [cm]	M_{PL} [cm]	*MLT* [cm]	W_t [kg]	c_v [dm^3]
28,6	13,7	1,4	20,4	20,0	43,6	5,1	0,6

A secondary winding comprised of 30 turns of a 2 mm copper conductor with isolating insulation equip the transformer core. Since the length of the transformer is less than one third of the long UI transformer, the total *MLT* is also comparatively small. Hence, total copper losses will be a fraction of those expected in the previously described transformer.

4.3.1 Magnetic permeability test

The magnetic permeability of the material in which the UU core is built can be estimated by operating an analogous test to that of sub-Sections 4.1.1 and 4.2.1. The RC low pass integrator probe is connected to the secondary in order to receive the time varying flux. Simultaneously, the primary current is registered to access the magnetic field to which the core is being subjected.

Figure 4.10 is the $B - H$ loop or hysteresis cycle that was obtained for the UU core. It is similar to the typical silicon steel $B - H$ loop, as seen in Figure 3.1(a), but in this case the loop is significantly sheered. This is most likely due to a residual air gap that exists in this core stack.

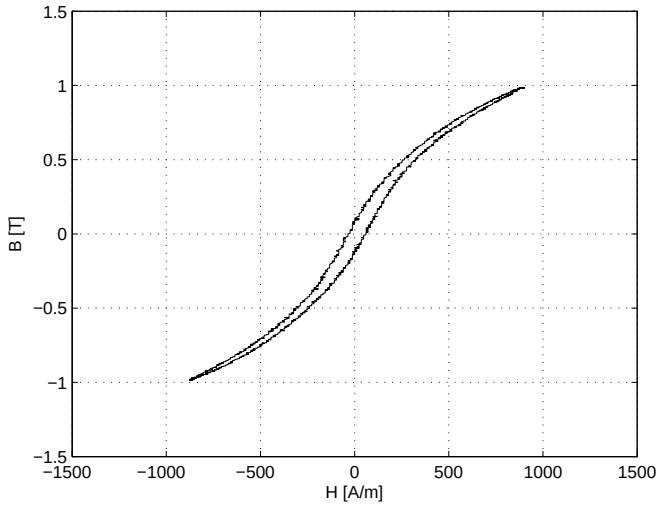

Figure 4.10: B-H loop for UU core.

The core in itself evidences a significantly low core loss as is perceived from the area contained inside the hysteresis cycle of Figure 4.10. Comparatively, the UU core is built in a material that is the most efficient of the three transformers described in this Chapter.

With a coercivity of $H_c \approx 60$ A/m and a magnetic flux remanence of $B_r \approx 0,11$ T the material can be considered to be magnetically *soft*. In this regard it demonstrates to be a material with better properties than that of the long UI transformer, as discussed in sub-Section 4.2.1, being especially suited for tasks that generate alternating fields.

On the other hand, since the maximum magnetic flux density of operation is $B_{max} \approx 0,99$ T, this transformer has a smaller potential to raise the output power than the long UI transformer. The impact of this property on the output power has been discussed in Section 3.4 and is evident in Figure 3.8(a). A higher magnetic flux density would then result in an increase of output power of the transformer.

The maximum relative magnetic permeability is estimated through the derivative below saturation in the $B - H$ loop of Figure 4.10. The value that was calculated for the UU transformer core is $\mu_{r_{max}} = 1664$.

4.3.2 Open circuit and short circuit tests

The open circuit test is performed using the same principles as described in sub-Section 4.1.2. The result of the experimental procedure is shown in Figure 4.11 which contains the open circuit voltage and current that were registered for the UU transformer.

Upon performing measurements of the *rms* magnitudes for the open circuit voltage and current, the values obtained are: $V_{oc} = 2,77$ V, $I_{oc} = 10,47$ Aand the open circuit power measured at $P_{oc} = 0,46$ W.

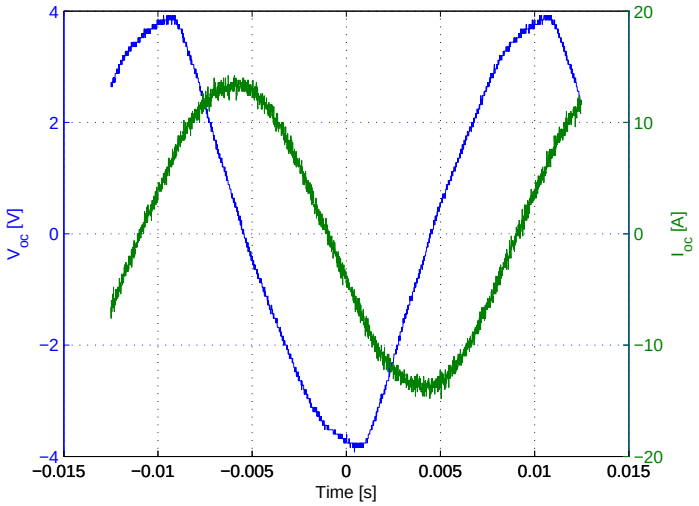

Figure 4.11: Open circuit voltage (blue) and current (green) for the UU transformer.

With the measurements taken above and knowing that the same principles that originated expression 4.1 are in effect, the impedance of the magnetizing branch is given by:

$$R_c = \frac{V_{oc}^2}{P_{oc}} = 16,9 \text{ m}\Omega \tag{4.21}$$

$$Z_\phi = \frac{V_{oc}}{I_{oc}} = 8,4 \text{ m}\Omega \tag{4.22}$$

$$X_m = \frac{1}{\sqrt{(1/Z_\phi)^2 - (1/R_c)^2}} = 9,7 \text{ m}\Omega \rightarrow L_m = 31,03 \ \mu\text{H} \tag{4.23}$$

The resistive part of the magnetizing branch is related to the power dissipated in the transformer core, in which case the core loss is expressed through:

$$P_{fe} = P_{oc} = V_{oc}^2/R_c = 0,46 \text{ W} \tag{4.24}$$

which indicates an efficient transformer core since this value is the lowest of the three transformers. Its also consistent with the hysteresis loops that were gathered for the three transformers, since the UU transformer $B - H$ loop, shown in Figure 4.10, is also the one with the lowest area enclosed inside the loop, which is directly related to low core losses.

An important use of the magnetizing inductance is to enable the computation of an relative magnetic permeability. Using the value gained in expression (4.23) equates a magnetic perme-

ability of $\mu_r \approx 59$. This value is significantly lower than the value calculated in sub-Section 4.3.1 and can only indicate that the open circuit test was performed in a region very close to saturation in the $B - H$ loop of Figure 4.10.

The result of the short circuit test is denoted in Figure 4.12. The test was performed by following the same procedure as described in sub-Section 4.1.2.

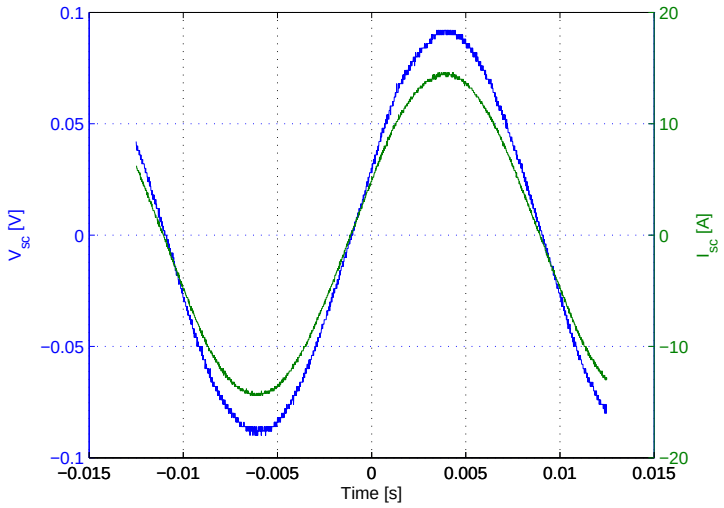

Figure 4.12: Short circuit voltage (blue) and current (green) for the UU transformer.

The magnitudes for the *rms* short circuit voltage and current are, respectively, $V_{sc} = 62,0$ mV, $I_{sc} = 9,8$ A and the short circuit power for this test was measured at $P_{sc} = 0,6$ W.

The equivalent impedance seen from the primary winding is set by expression (4.6) and is computed using the measurements taken from the short circuit test as follow:

$$Z_{sc} = \frac{V_{sc}}{I_{sc}} = 6,3 \text{ m}\Omega \tag{4.25}$$

$$R_{sc} = \frac{P_{sc}}{I_{sc}^2} = 193,7 \text{ m}\Omega \tag{4.26}$$

$$X_{sc} = \sqrt{Z_{sc}^2 - R_{sc}^2} = 193,6 \text{ m}\Omega \rightarrow \frac{X_{sc}}{\omega} = L_m || L_{l_s}^{'} = 616,14 \ \mu\text{H} \tag{4.27}$$

A leakage flux coefficient that lumps together the leakage flux in the transformer windings is computed through the following expression:

$$L_s^{'} = -\frac{(L_m || L_{l_s}^{'}) \cdot L_m}{(L_m || L_{l_s}^{'}) - L_m} = 32,68 \ \mu\text{H} \tag{4.28}$$

The total copper loss in the transformer windings is approximated by the short circuit resistance that represents an equivalent resistance in the impedance seen from the primary winding:

$$P_{cu} = P_{sc} = R_{sc} I_{sc}^2 = 0,6 \text{ W} \tag{4.29}$$

that is expected given that the UU transformer has a significantly lower *MLT*, as seen in Table 4.3, comparatively with the long UI transformer, expressed in Table 4.2.

5

Load tests and resonant circuit

This chapter is dedicated at performing and showing the results of extensive load tests to the transformers described in Chapter 4. The load tests are executed by varying both the transmission line current and the resistive load attached to the transformer to simulate the RIOL robot.

Furthermore, simulations based on the models presented in Chapter 3 are done following the procedure enumerated in Section 3.4. The necessary dimensional and electromagnetic data for the models is gathered in Chapter 4.

The values acquired through simulation are then matched against the collected field data in order to validate the transformer models and the electromagnetic parameters that were obtained through the tests of Chapter 4.

Subsequently, a capacitor is connected to the secondary winding in order to establish a resonant circuit. A model is derived for this case as well as the principles of operation of the resonant circuit. Load tests are performed in order to experimentally determine the value of the capacitor that maximizes the output power.

A load test for the peak primary current is repeated and the output power results are compared with the case without capacitor as a means to unravel the impact of the resonant circuit. Finally, a simulation of the transformer with the resonant circuit is carried out in order to validate the models that were developed for this case.

5.1 Load tests

The load test is carried out by imposing a primary current, that represents the transmission line current seen in the transformer primary circuit, and connecting a pure resistive variable load to the secondary circuit. A primary winding is run through the transformer window in order to simulate the transmission line. Contrary to the option taken in [7], the primary winding has only one turn instead of the three utilized in that work.

A transformer primary circuit with only one turn for the primary winding is more coherent with the real situation when the RIOL is positioned in a transmission line cable. Furthermore, inspecting expression 3.14 makes it clear that using three turns will be more beneficial since it results in a lower magnetizing current. Using one turn avoids that and therefore is a more accurate approximation to the actual real case.

A laboratory apparatus was constituted in order to obtain the values desired for the primary current. In this case the values were between 50 A and 350 A, so that a range of primary current values could be used in the load tests. Greater values were deemed unachievable due to technical limitations in the laboratory. Notice that a value around 300 is most likely the probable worst case scenario considering the current profile of a transmission line. The laboratory set-up and technical details to achieve a primary current of 350 A are described in Appendix A.1.

In order to evaluate the transformers described in Chapter 4, the primary current is changed in steps of 50 A, starting at 50 A and ending in 350 A. For each step the variable resistive load is changed along the range of $0,5\ \Omega$ to $5\ \Omega$ in $0,5\ \Omega$ steps. Finally, in each step, a search for the optimum value of the resistive load is performed. Measurements of the primary and secondary voltage and secondary current are taken during this iterative procedure along with a measurement for the output power of the transformer and corresponding power factor.

Afterwards, the same values for the primary current and the resistive load are inserted into the models developed in Section 3.3 along with the dimensional and electromagnetic data for each transformer of Chapter 4. In this way, the procedure of Section 3.4 is followed with the physical data being imposed from Tables 4.1, 4.2 and 4.3. The electromagnetic parameters intrinsic to each transformer are drawn from the results of the magnetic permeability tests and the open circuit and short circuit tests that were applied to the transformers of Chapter 4.

The computer simulations are carried out in order to obtain the predicted values for the output power of each transformer under the same premisses as the laboratory load tests. Emphasis is given to output power since this variable is linked to the most important design goal of the transformer that is defined in Section 3.1. The field data gathered for each transformer is then confronted against the predicted values of each model in order to establish the most accurate model as well as draw conclusions about the importance of relevant physical and electromagnetic parameters of the transformer.

5.1.1 Short UI transformer

The short UI transformer is submitted to load testing with the input current injected in the primary winding and the variable resistive load connected to the secondary winding. The results of varying the primary current while changing the value of the resistive load seen from the secondary winding are expressed in Figure 5.1. The output power is shown for each value of the primary current across a range of values for the resistive load.

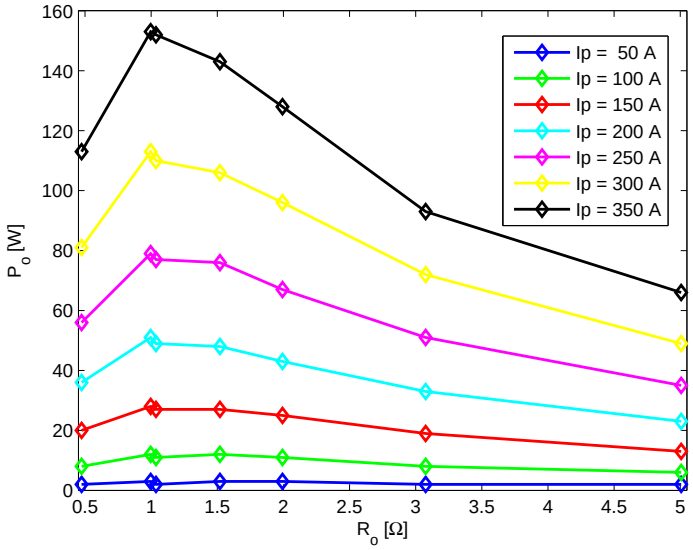

Figure 5.1: Measured output power for a varying primary current and load resistance (short UI transformer).

Figure 5.1 demonstrates that the higher the input current, the higher the output power, which is to be expected. It also shows that for this transformer there is a load value that maximizes the output power.

In this case the value is approximately $R_o = 1\ \Omega$, which translates to a maximum value of the output power in each value of the primary current. Past that value, the output power significantly decreases as the value of the resistive load increases since the secondary current is also substantially diminished and is not compensated by the rise in the secondary voltage.

The point where the load connected to the secondary winding of the transformer reaches its optimum value is of interest since it dictates the maximum power output of the transformer. As seen in Figure 5.1, the maximum output power value is situated in the case were $I_p = 350$ A.

Measurements of the secondary voltage and current are registered after carefully varying the resistive load to the point were it maximizes the output power. Figure 5.2 displays the time variant secondary voltage and current at precisely that point.

Upon inspection, it can be seen that the transformer is not saturated and the secondary voltage is in phase with the secondary current, which expresses a unity power factor. At this point the maximum output power of the short UI transformer is measured at $P_{o_{max}} = 153$ W.

On the other hand, the measured *rms* values for the primary voltage and current are, respectively, $V_p = 2,48$ V and $I_p = 356,38$ A. The measured input power was $P_i = 302$ W, which translates to a transformer efficiency of $\eta \approx 51\%$ and a core and copper loss of $P_\Sigma = 149$ W.

The value for the maximum output power is relatively low in comparison with the targeted value by the specifications (around 1 kW). It reflects the fact that the transformer has a large M_{PL}, which enhances the magnetizing current and therefore impairs the output power of the transformer. Furthermore, the load tests also authenticate the significant core loss and substantial leakage flux that characterize this transformer as revealed by the tests in Section 4.1.

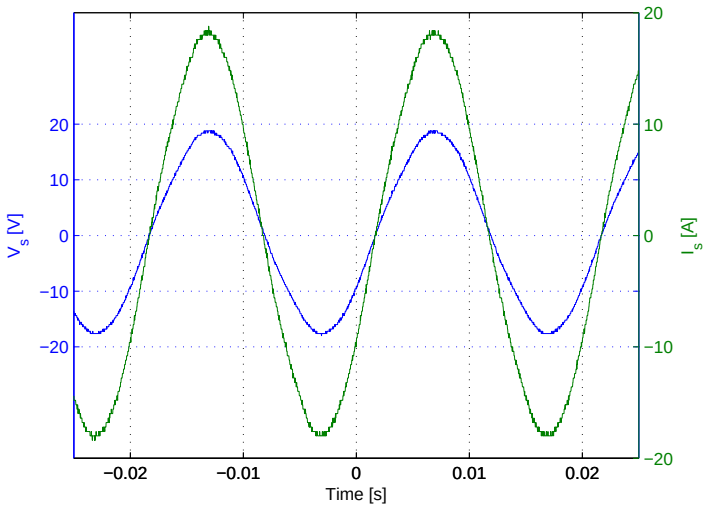

Figure 5.2: Measured secondary voltage and current, primary current of 350 A and optimum load (short UI transformer).

In order to evaluate the models described in Chapter 3, the output power for this transformer is computed for three models: the no leakage flux and optimum load of sub-Section 3.3.1, the no leakage flux and variable load of sub-Section 3.3.2 and the leakage flux and variable load model of sub-Section 3.3.3.

The case with a primary current of 350 A is chosen as a term of comparison and then all values are plotted in Figure 5.3. The results for the model of no leakage flux and optimum load are not shown since it produced imaginary values as the magnetizing current term in expression (3.10) turned to overcome the primary current term.

Figure 5.3 demonstrates that both models of Sections 3.3.2 (in red) and 3.3.3 (in green) are valid for representing the measured case (in black). The models predict the response of the output power along the range of values attributed to the resistive load connected to the secondary. The more simpler model of Section 3.3.1, that was developed in [7], is unfit to model the real case since it produces invalid solutions with the same input data as the previously cited models.

The most accurate model, comparatively, is the one which also characterizes the leakage flux phenomenon, being a necessary term in order to closely approach the measured values. This model also determines the peak output power with significant accuracy.

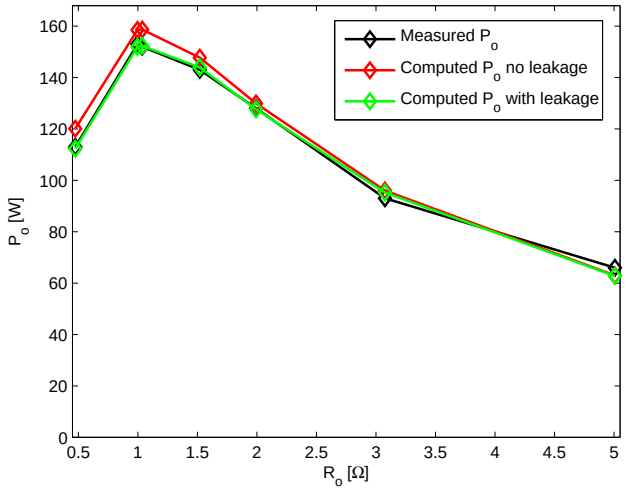

Figure 5.3: Measured output power versus computed output power for a primary current of 350 A (short UI transformer).

It can be seen, by inspecting the output power expressions (3.16) and (3.21), that if there was no leakage flux present in the real case, both models would produce the same result. In that case, using the same dimensional data for the transformer, the magnetic permeability term would be the deciding factor in approaching the measured values since it determines the magnetizing current term influence.

Furthermore, as expected from conclusions drawn in sub-Section 3.3.3, it can be recognized from Figure 5.3 that as the resistive load increases, the magnetizing current and leakage flux terms loose importance in the output power expressions. Hence, as seen in Figure 5.3 for values greater than $R_o = 4\,\Omega$, both models present the same value and start to detach from the measured values.

5.1.2 Long UI transformer

The variable resistive load is connected to the secondary winding of the long UI transformer and a primary current is imposed in order to perform the load tests. Figure 5.4 represents the effect on the output power of varying the primary current while going through steps of the variable resistive load.

It can be observed that in this case, besides a higher primary currents resulting in a higher output, which is to be expected, that the output power increases steadily with the increment of the resistive load. This behaviour is significantly different from the one encountered in the short UI transformer of sub-Section 5.1.1, were there was a clear optimum value for the resistive load which boosted the output power.

The tests were stopped around $R_o \approx 18\,\Omega$, since beyond that value it was no longer possible to impose a primary current to the transformer because the reaction of the secondary circuit was affecting the primary winding, effectively lowering and limiting the value of the primary current.

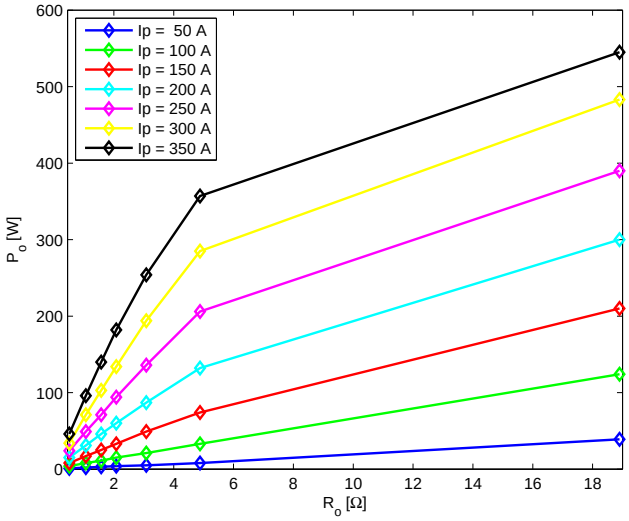

Figure 5.4: Measured output power for a varying primary current and load resistance (long UI transformer).

Figure 5.4 demonstrates that it was not possible to perceive an optimum value for the resistive load. Hence, there is only a point of measured maximum output until it was possible to guarantee a primary current value of $I_p = 350$ A. Inspecting Figure 5.4 reveals that $P_{o_{max}} = 545$ W, which is a relatively satisfactory in regards to the 1 kW target since this value is registered for a primary current that is in the lower range of a typical transmission line current.

Through extrapolation of the behaviour of the output power and the impact of increasing the primary current seen in Figure 5.4, it is expected that with a primary current in the range of 600 A the increase in output power would be significant.

The measurements taken for the secondary voltage and current, in the case were the primary current is $I_p = 350$ A and the variable load is $R_o = 2\ \Omega$, are displayed in Figure 5.5. In this particular set-up the output power of the transformer is measured at $P_o = 182$ W.

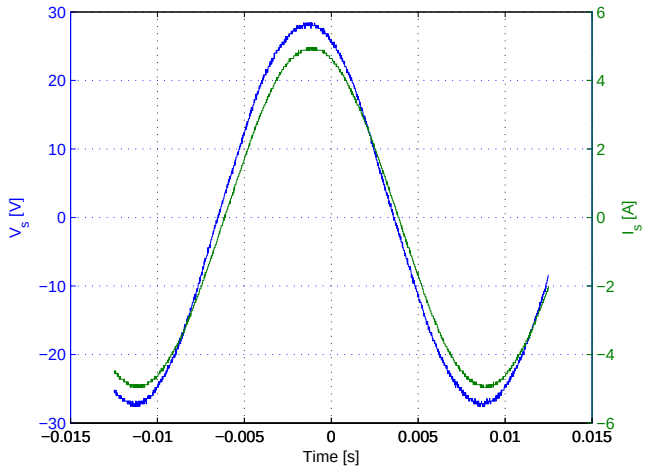

Figure 5.5: Measured secondary voltage and current, primary current of 350 A and $2\ \Omega$ load (long UI transformer).

The c ase of Figure 5.5 is selected because it was not possible to reach a situation of optimum load with the primary current still imposed. This was due to limitations in the auxiliary transformer producing the primary current.

In order to assess transformer efficiency, the measurements of the *rms* values for the primary voltage and current are $V_p = 1,01$ V, $I_p = 350,73$ A and the measured power supplied to the transformer is $P_i = 349$ W. Thus, the corresponding efficiency is $\eta \approx 52\%$. Under these conditions, the combined core and copper loss dissipated in the transformer is $P_\Sigma = 167$ W.

A comparison featuring the measured and computed transformer output power for a case with a primary current of 300 A is presented in Figure 5.6. As with the short UI transformer, the simplified model of sub-Section 3.3.1 fails to produce valid results for the output power.

Figure 5.6 reveals that for this transformer the model without flux leakage coincides with the simulated values for the model with flux leakage. This occurs because the long UI transformer features a relatively small M_{PL} in relation to the amount of leakage flux it possesses, which is influential in the output power formulations, (3.16) and (3.21), used for simulation.

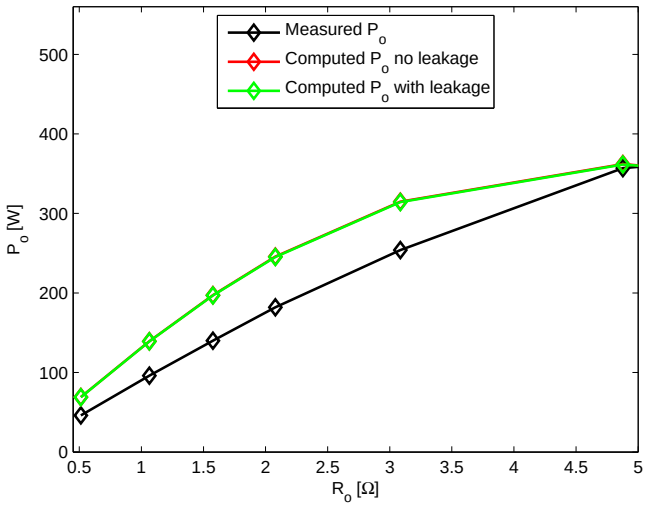

Figure 5.6: Measured output power versus computed output power, primary current of 350 A (long UI transformer).

Both models, with and without leakage flux, overestimate the value of the output power across the range of the resistive load used in the test. A possible explanation is linked to the magnetic permeability value since in this case the transformer is saturated and thus the real value is certainly lower than the predicted one.

Nevertheless, both models coincide with the maximum measured output power. That fact happens when the value of the resistive load has more influence over the output power than the magnetizing current term in expressions (3.16) and (3.21).

5.1.3 UU transformer

The load tests are performed in accordance with the procedures applied in sub-Sections 5.1.1 and 5.1.2. The output power response in the UU transformer is displayed in Figure 5.7. As with the short UI transformer, the output power rises along with the load resistance up to an optimum point and then decreases as the load resistance is incremented. The maximum output power is achived between $2,0\ \Omega$ and $3,5\ \Omega$, depending on the case of the primary current.

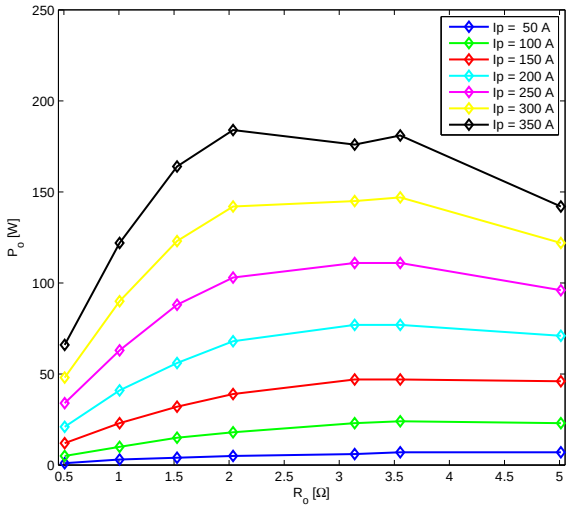

Figure 5.7: Measured output power for a varying primary current and load resistance (UU transformer).

By looking at the output power expression in (3.21), where the load resistance is present on its own and as part of the magnetizing current term, there is a clear relation with the measured values. This relationship is based on the fact that up to an optimum value, the load resistance term is balancing the magnetizing current term effect and augments the output power. Past that point, the load resistance indication present in the magnetizing current term forces the decrease in the output power as seen in Figure 5.7.

The maximum measured output power for the UU transformer was registered under a primary current of 350 A and a $2\ \Omega$ load. The value retrieved from Figure 5.7 is $P_{o_{max}} = 184$ W. At the same point of operation, the secondary voltage and current is also registered and presented in Figure 5.8. Its evident from observing Figure 5.8 that this point of operation is not the exact location, albeit in the vicinity, for the optimum load since the secondary current is not perfectly in phase with the voltage.

A measurement was also taken of the *rms* values for the primary voltage and current, which are, respectively, $V_p = 0,79$ V and $I_p = 350,73$ A. The power delivered to the transformer was measured at $P_i = 212$ W. Thus, because the output power registered at this point is 184 W, the aggregated core and copper losses are estimated at $P_\Sigma = 28$ W. This translates to a transformer efficiency of $\eta \approx 87\%$, which is the highest of the tested transformers in this chapter.

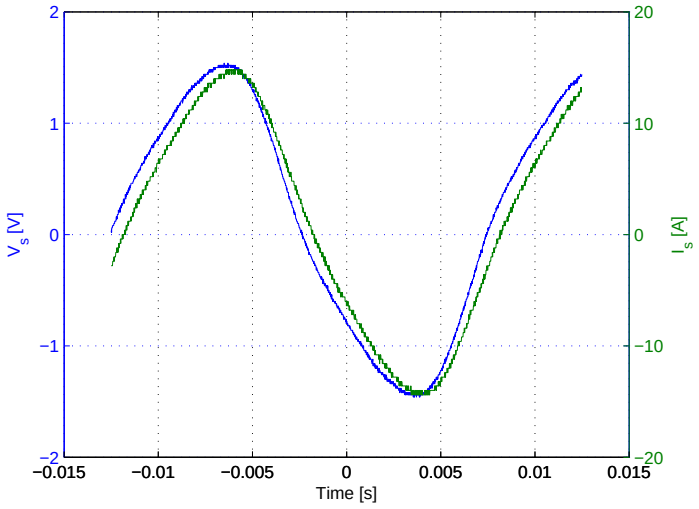

Figure 5.8: Measured secondary voltage and current, primary current of 350 A and $2\ \Omega$ load (UU transformer).

The case in which the primary current is 350 A is selected to establish a comparison between the measured values and the values computed through the transformer models of Section 3.3. Both the measured and the corresponding computed values are shown in Figure 5.9.

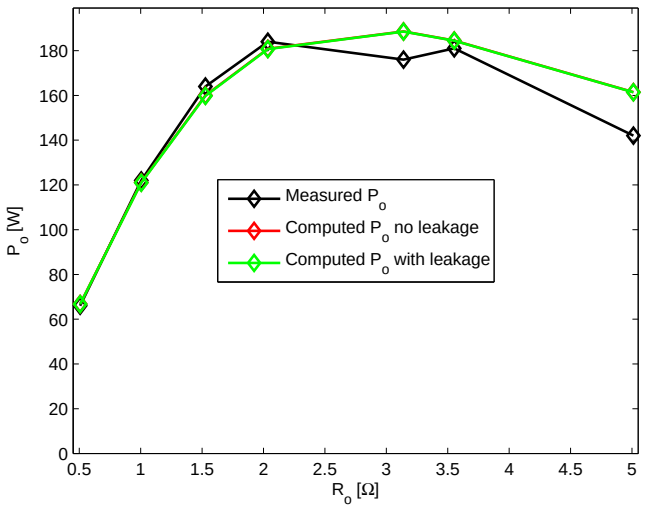

Figure 5.9: Measured output power versus computed output power, primary current of 350 A (UU transformer).

A first observation of Figure 5.9 exposes the fact that the computed model with no leakage closely follows the model which has a representation of leakage flux. This already occurred with long UI transformer as stated in sub-Section 5.1.2 and is explained by low leakage flux in the transformer and a small M_{PL}.

The ratio of the magnetic path length, M_{PL}, and the magnetic permeability, μ, of the transformer is a decisive physical characteristic that significantly determines the magnetizing current level and therefore its influence in the output power of the transformer.

Figure 5.9 also shows that the computed values are accurate up to a point were the transformer starts to saturate. In this case up to around $2\ \Omega$, were it was found that the transformer is in pre-saturation. Past that point the models begin to have a slight difference towards the measured values, that accentuates as the load increases and the saturation level is higher.

The measured secondary voltage and current of the transformer for an input current of 350 A and a load of $5\ \Omega$ are displayed in Figure 5.10. Inspecting it clearly demonstrates that for a $5\ \Omega$ load the transformer is saturated and therefore the magnetic permeability value is in reality significantly lower than if it was not saturated.

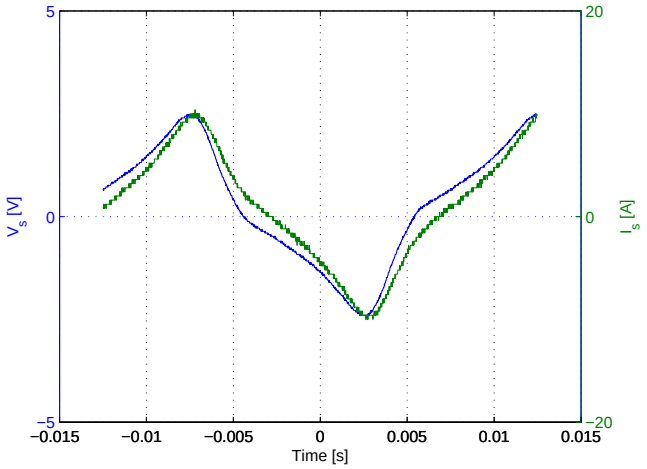

Figure 5.10: Measured secondary voltage and current, primary current of 350 A and $5\ \Omega$ load (UU transformer).

The transformer models utilized to compute the simulated values use a magnetic permeability value determined in Chapter 4 for a non-saturated case. Hence, when computing the output power for values above $2\ \Omega$, the magnetic permeability is relatively higher than the one in the measured case, which explains the difference between values observed in Figure 5.9.

5.2 Resonant circuit

The output power of the transformers that was measured in Section 5.1 is insufficient to support the RIOL power needs. Increasing the core volume of the transformers, by either incrementing the core cross-section, A_c, or the length of the transformer, l_c, is not an option since that augments weight. A possible solution to boost the output power without physically altering the transformers is by way of a resonant circuit.

In order to produce a resonant circuit a capacitor is connected in parallel with the secondary winding of the transformer. The objective is to compensate the inductance value originated from the magnetizing inductance and the leakage flux inductances. Accordingly, the capacitor has to be sized to match the total inductance seen from the secondary winding.

For a given frequency, known as the resonant frequency, the impedance of the LC circuit is theoretically infinite and it acts as a band pass circuit. In this condition the primary current flows directly to the secondary winding, with the magnetizing current being effectively minimized.

For this case, the transformer is represented by the equivalent circuit of Figure 5.11 which disregards the winding resistances and lumps the leakage flux into a inductance that is reduced to the primary circuit.

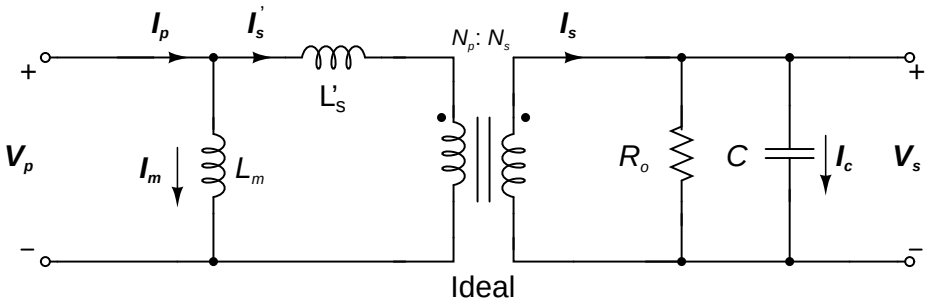

Figure 5.11: Transformer equivalent circuit with capacitor.

A demagnetizing current is introduced into the transformer and the reactance associated with the magnetizing branch, X_m, is balanced by the imposed capacitor reactance X_c, which injects reactive power to the transformer circuit.

The adequate capacitor can be estimated by resorting to simplifications which arrive to specific cases of the general case exposed in Figure 5.11. A straight forward approach disregards the load resistance and the leakage flux parameter, leaving the transformer represented by the magnetizing inductance. This is exemplified in Figure 5.12, that shows the circuit completely referred to the primary side.

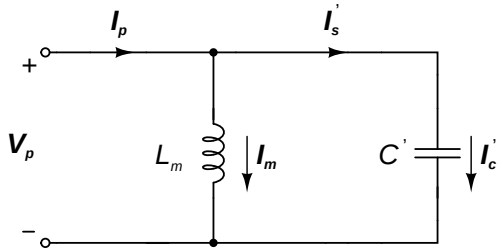

Figure 5.12: Equivalent circuit with magnetizing inductance and capacitor.

The equivalent impedance of the circuit is provided by the parallel of the magnetizing inductance with the capacitor, hence it can be expressed as:

$$\bar{Z}_{eq} = \bar{Z}_{L_m} \parallel \bar{Z}_{C'} = -\frac{\jmath\omega L_m}{\omega^2 L_m C' - 1} \tag{5.1}$$

In order to achieve an infinite impedance, the following relation must be complied:

$$\lim_{\omega^2 L_m C' \to 1} Z_{eq} = \infty \Rightarrow \omega^2 L_m C' - 1 = 0 \tag{5.2}$$

The value of the capacitor for this specific case is obtained directly from expression (5.2) as a function of the frequency and the magnetizing inductance:

$$C^{'} = \frac{1}{\omega^2 L_m} \tag{5.3}$$

which can be referred back to the secondary side using relation (2.19) as $C = C^{'} n^2$ since the capacitor is connected to the secondary winding.

As such, with a capacitor given by (5.3) the circuit is in resonance and has an associated resonance frequency which is derived from (5.3) as:

$$f_r = \frac{1}{2\pi\sqrt{L_m C'}} \tag{5.4}$$

Another possible simplified circuit retrieved from the equivalent circuit shown in Figure 5.11 is exposed in Figure 5.13 which is strictly referred to the primary side. In this particular case the transformer is represented by the magnetizing inductance and by a leakage flux inductance that lumps together the various leakage flux components. The effect that the load resistance has on the transformer is disregarded.

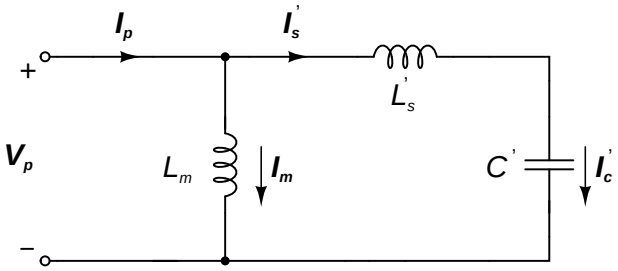

Figure 5.13: Equivalent circuit with magnetizing inductance, leakage flux inductance and capacitor.

The circuit of Figure 5.13 has an equivalent impedance given through the parallel of the magnetizing inductance, L_m with the series of the capacitor, $C^{'}$, and the leakage flux inductance, $L_s^{'}$. Therefore, it can be written as follows:

$$\bar{Z}_{eq} = \bar{Z}_{L_m} \parallel (\bar{Z}_{C'} + \bar{Z}_{L_s'}) = -\frac{\jmath\omega(L_m - \omega^2 L_m L_s^{'} C^{'})}{\omega^2 C'(L_m + L_s') - 1} \tag{5.5}$$

which follows an analogue rule to expression (5.2) in order to achieve a resonant equivalent impedance with an infinite value dictated by:

$$Z_{eq} \to \infty \Rightarrow \omega^2 C^{'}(L_m + L_s^{'}) - 1 = 0 \tag{5.6}$$

The value of the capacitor that enables the circuit to reach a resonant frequency is obtained by solving relation (5.6) as follows:

$$C^{'} = \frac{1}{\omega^2(L_m + L_s')} \tag{5.7}$$

which is equal to the value encountered for the case without leakage flux inductance, as seen in expression (5.3), if there is no leakage flux in the transformer, that is $L_s^{'} = 0$.

The third simplified circuit is reached by adding in the load resistance in parallel with the secondary winding and the capacitor. On the other hand, it features the magnetizing inductance but disregards the leakage flux component since the focus is to demonstrate the effect of considering the load resistance in the model. The resulting circuit is indicated in Figure 5.14.

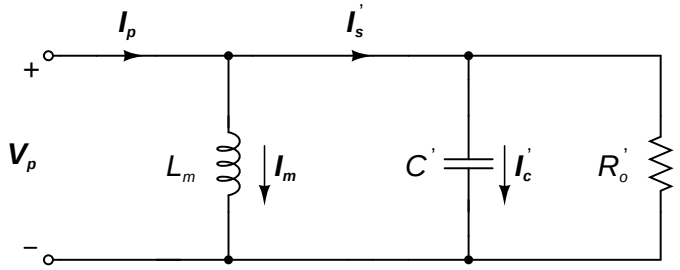

Figure 5.14: Equivalent circuit with magnetizing inductance, load resistance and capacitor.

A equivalent impedance is established by associating the load resistance and the capacitor in parallel and then combining the result in parallel with the magnetizing inductance. Hence, the circuit of Figure 5.14 has a equivalent impedance expressed by:

$$\bar{Z}_{eq} = \bar{Z}_{L_m} \parallel (\bar{Z}_{C'} \parallel \bar{Z}_{R_o'}) = -\frac{\jmath\omega L_m R_o^{'}}{\omega^2 L_m C' R_o' - \jmath\omega L_m - R_o'} \tag{5.8}$$

where the capacitor and load resistance are referenced back to the secondary winding by means of $C = n^2 C^{'}$ and $R_o = n^2 R_o^{'}$.

As before, the circuit is in resonance when the equivalent impedance follows a similar expression dictated by (5.2) in which the impedance is infinite when:

$$Z_{eq} \to \infty \Rightarrow \omega^2 L_m C^{'} R_o^{'} - \omega L_m - R_o^{'} = 0 \tag{5.9}$$

The value of the capacitor that is related to the resonance condition is obtained by solving (5.9). After rearranging terms the capacitor is given by:

$$C^{'} = \frac{\omega L_m + R_o^{'}}{\omega^2 L_m R_o^{'}} \tag{5.10}$$

To complete the analysis, the last option is to consider all components of the circuit in Figure 5.11. The circuit is reduced to the primary side of the transformer and is shown in Figure 5.15.

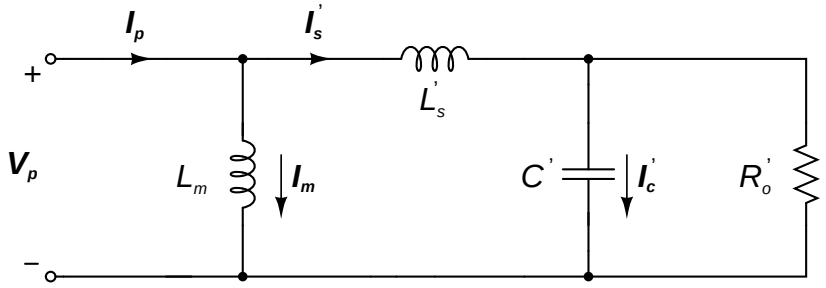

Figure 5.15: Equivalent circuit with magnetizing inductance, leakage flux inductance, load resistance and capacitor.

The circuit as an equivalent impedance that is originated by the parallel of the magnetizing inductance with the series of the lumped leakage flux inductance with the parallel of the load resistance and the capacitor. The resultant impedance is expressed as:

$$Z_{eq} = Z_{L_m} \parallel (Z_{L_s^{'}} + Z_{C'} \parallel Z_{R_o^{'}}) = \frac{\jmath(\omega L_m R_o^{'} - \omega^3 L_m L_s^{'} C' R_o^{'}) - \omega^2 L_m L_s^{'}}{R_o^{'} - \omega^2 C' R_o^{'}(L_m + L_s^{'}) + \jmath\omega(L_m + L_s^{'})} \tag{5.11}$$

In this case the capacitor is also found by applying a similar procedure as in (5.2), which enables the following expression:

$$|Z_{eq}| \to \infty \Rightarrow R_o^{'} - \omega^2 C' R_o^{'}(L_m + L_s^{'}) + \omega(L_m + L_s^{'}) = 0 \tag{5.12}$$

The capacitor that produces an equivalent impedance of infinite value is found by solving (5.12). After rearranging terms, the capacitor is given by:

$$C' = \frac{R_o^{'} + \omega(L_m + L_s^{'})}{\omega^2 R_o^{'}(L_m + L_s^{'})} \tag{5.13}$$

which is reduced to the expression found in (5.10) if there is no leakage flux in the transformer and therefore $L_s^{'} = 0$.

5.2.1 Resonant circuit simulation

The resonant circuit principle is simulated as a mean to predict the capacitor value and it's impact on the output power of a transformer. The long UI transformer described in Section 4.2 is selected for this simulation as it is the transformer that measured the highest output power in the load tests of Section 5.1.

As a starting point, the models presented in Section 5.2 are employed to gauge the capacitor value that is adequate to this specific transformer. The data required for the computation is gathered in the results of the open and short circuit tests applied to the long UI transformer in sub-Section 4.2.2.

Beginning with the simplest model, the value of the capacitor is obtained from expression (5.3), resulting in a value of $C_1 \approx 24$ μF. The next model differs by also considering leakage flux and therefore the value of the capacitor is drawn from relation (5.7), producing a value of $C_2 \approx 23$ μF.

The third model disregards the leakage flux but contemplates the influence of the load resistance in expression (5.10), consequently, the value of the capacitor that results from this method is $C_3 \approx 128$ μF. The forth and most complete model is based on considering the effects of the leakage flux and the load resistance, which, through (5.13), produces a value of $C_4 \approx 126$ μF.

Two direct conclusions are drawn from the values of capacitor C_1 to C_4. Firstly, the models that consider a leakage flux inductance register slightly lower values in regard to their comparable model, that is C_2 to C_1 and C_4 to C_3. The second fact is that modelling the load resistance significantly increases the value of the capacitor, which leads to a conclusion that contemplating the load resistance is necessary to obtain valid results.

A Matlab/Simulink model is developed in order to further investigate the optimum capacitor value for the long UI transformer. Figure 5.16 presents the block diagram used to model the transmission line coupled with the transformer, which has an attached capacitor and the load resistance to model the RIOL.

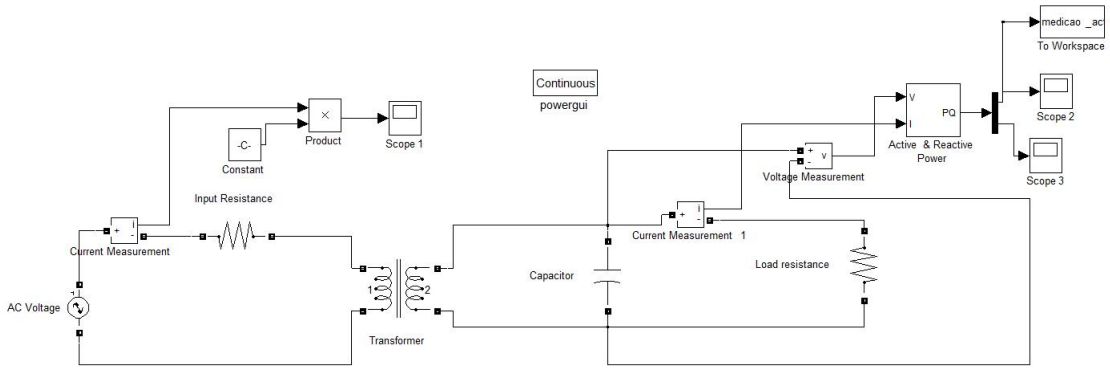

Figure 5.16: Load test block diagram of transformer with capacitor.

A series of simulated load tests are performed through the model of Figure 5.16 by varying the capacitor value in $5\ \mu$F steps. By following this procedure it was possible to measure the impact on the output power of each value that is assigned to the capacitor. The results of this series of simulated load tests are displayed in Figure 5.17.

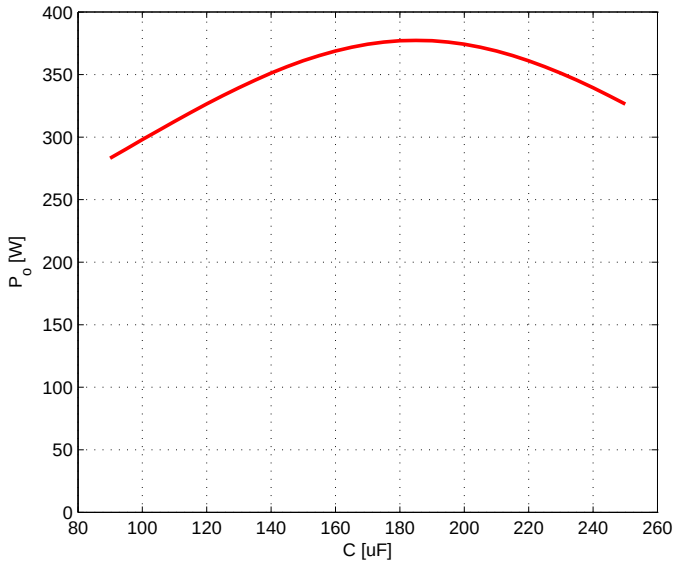

Figure 5.17: Output power versus the capacitor value for the long UI transformer.

Through the observation of Figure 5.17 it can be stated that the long UI transformer has a optimum value for the capacitor situated at the $185\ \mu$F mark. This value has now to be assessed experimentally in order to determine the validity of the models and simulation.

5.2.2 Load tests with capacitor

The resonant circuit principle is tested on the transformer that provided the highest value of output power in the load tests carried out in Section 5.1, which is the long UI transformer.

After connecting the capacitor to the secondary winding, a series of load tests are performed as a means to experimentally determine the value of the capacitor that maximizes the output power of the long UI transformer for a set primary current.

A primary current of 150 A is used throughout this test because of limitations in the auxiliary transformer that is used to generate the primary current. Basically the transformer could not guarantee a fixed value for the primary current throughout the duration of the test since it overheated rapidly if a higher primary current was requested. Nevertheless, a few isolated tests for higher values of the primary current were performed in order to establish the maximum output power of the tested transformer when the optimum capacitor was connected.

The output power of the transformer is thus measured while varying the value of the capacitor with the load resistance set in the optimum value for each case. The results of this test are displayed in Figure 5.18.

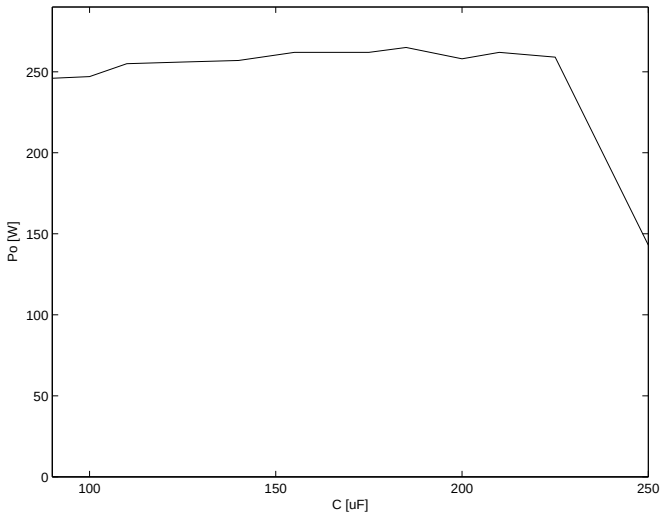

Figure 5.18: Measured output power as a function of the capacitor (long UI transformer).

As seen in Figure 5.18, the capacitor is varied from 90 μF to 250 μF, a point were it was evident that increasing the capacitor would only further diminish the output power.

Inspecting Figure 5.18 reveals that the maximum value of output power, 265 W, is registered when the capacitor is valued at 185 μF. This value is in concurrence with the value obtained through simulation from Figure 5.17.

On the other hand, the values computed through the models, C_1 to C_4, in sub-Section 5.2.1, are substantially detached from the experimental value. C_1 and C_2 have a greater difference than C_3 and C_4, which shows that modelling the load resistance is necessary to put the predicted capacitor value in the same order of magnitude as the experimental value.

Up to 185 μF, an increase in the capacitor value translated into an increase in output power, a fact that was not predicted in simulation as is denoted in Figure 5.17. Beyond 185 μF and up to 225 μF the output power slightly decreases and stagnates around 260 W, after which the output power plunges as the capacitor is increased, which was expected from the simulation.

Following these results, the experimental value of 185 μF is set as the optimum capacitor adapted to the long UI transformer. Subsequently, the primary current is set at a maximum of 350 A and the load resistance regulated to the optimum point that maximizes the output power. The resultant secondary voltage and current are denoted in Figure 5.19, where it can be seen that both voltage and current have a significant harmonic content due to the introduction of the capacitor.

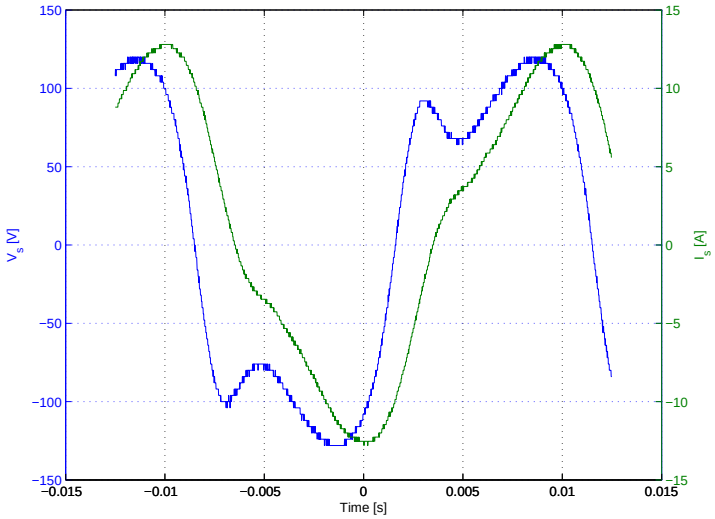

Figure 5.19: Measured secondary voltage and current, primary current of 350 A and capacitor of 185 μF.

The measured output power for the case of Figure 5.19 is $P_o = 635$ W. As displayed in Figure 5.4, for the case with a primary current of 350 A and an optimum load, the maximum output power drawn from the long UI transformer without the capacitor is $P_o = 545$ W. Therefore, the benefit of applying the capacitor is measured at 90 W or a 16% increase in the output power.

A second load test with the capacitor was also performed for a primary current of 300 A and optimum load for means of further comparison. The measured output power for this case was $P_o = 566$ W, with the *rms* values for the secondary voltage and current being, respectively, $V_s = 81,60$ V and $I_s = 6,98$ A. Referring back to Figure 5.4, the measured output power for the analogous case is $P_o = 483$ W. This establishes a differential of 83 W, which means the usage of the capacitor increased the output power by around 17%.

It should be noted that the experimental capacitor is not fine tuned, since it was only possible to vary the value of the capacitor in 10 to 25 μF steps. Hence, a more precise value for the capacitor would result in a higher output power, a point were the resonance frequency is reached.

6

Conclusion

6.1 Summary

An analysis of the type of transformer to supply the RIOL was carried out in this thesis. The purpose of developing and validating suitable transformer models by means of load tests and experimental work was achieved. A design procedure was enunciated based on the developed models and the general specifications that are needed for a valid transformer solution. Furthermore, the impact of installing a capacitor in order to produce a resonant circuit to boost the output power of the transformer was studied and measured. This was the result of a series of logical steps that were taken throughout the Chapters of the thesis.

The fundamental magnetic and electrical principles that govern the transformer are presented systematically in Chapter 2. The transformer operation principle is given through inductive coupling theory in order to express the relation between induced electromotive force and magnetic flux as described by Faraday's law.

A typical magnetization path for a material that forms the core of a transformer is presented and the effects of hysteresis and saturation are shown. Chapter 2 explains the origins of transformer losses and develops the concept of a equivalent circuit that addresses each non-ideality present in real transformers.

Chapter 3 enumerates the specifications and the design process of a transformer suitable to suplly the RIOL. The iterative design process notes and concurs that the transformers are designed for specific requirements, with judicious trade-off between specifications being made as optimum performance over a wide range of operation is not offered.

The material of choice for the transformer core is established after a thorough description and comparison of the magnetic materials available commercially. Silicon steel characteristics are explained and the specific properties of the various laminations that are available in the industry are discussed in more detail.

Transformer design models that are suitable for the representation of the transformer and RIOL are derived and a design algorithm is presented based on these models coupled with geometry considerations that are specific for the various possible transformer cores.

Each transformer is then presented in Chapter 4, were physical and electrical details are enumerated and key specifications are discussed. Core dimensions and physical characteristics are given and particular features are related to the performance of the transformer. A comparison between physical parameters of the transformers is enunciated as a means to discuss the most beneficial properties that are needed for a transformer suited to equip the RIOL robot.

Subsequently, the magnetic properties of the materials that compose the core of each transformer are studied and measured through a test devised to obtain the $B - H$ loop of the material in question.

Through the measured hysteresis loops, key features such as the magnetic permeability, the coercivity and remanence of the materials is evaluated and then compared against the values of typical industry standard materials.

The relevant open circuit and short circuit tests are also applied to each of the transformers in Chapter 4. With these, various electrical and magnetic parameters of the transformers are derived and related to the models in Chapters 2 and 3. Measurements are performed to estimate parameters of the transformer model, namely the the magnetizing inductance and resistance, the total leakage flux referred to the primary side, the winding inductances and resistances and the total copper loss.

The main part of Chapter 5 refers to the execution of extensive load tests that are applied to the transformers described in Chapter 4. The load tests are performed by varying both the transmission line current and the resistive load attached to the transformer to simulate the RIOL robot. The maximum output power retrieved from the short UI transformer was measured at $P_{o_{max}} = 153$ W, with a transformer efficiency of $\eta \approx 51\%$. The long UI transformer was able to deliver a maximum output power of $P_{o_{max}} = 545$ W at an efficiency of $\eta \approx 52\%$. The registered value for the maximum output power of the UU transformer was $P_{o_{max}} = 184$ W, with a transformer efficiency of $\eta \approx 87\%$.

The results of the load tests for each transformer are then used to validate the models and design procedure presented in Chapter 3. The simulated data is obtained by following the procedure enumerated in Section 3.4 and using the dimensional and electromagnetic data gathered in Chapter 4.

Through the load tests and the simulated data it is demonstrated that both models of Sections 3.3.2 and 3.3.3 are valid in terms of representing the measured cases. The simpler model of Section 3.3.1, that was developed in [7], is deemed unfit to model the real case since it produces invalid solutions with the same input data as the previously cited models.

Furthermore, it is shown that the most accurate model, comparatively, is the one which also characterizes the leakage flux phenomenon, being a necessary term in order to closely approach the measured values. This model also determines the peak output power with significant accuracy. On the other hand, the results also evidence that if the transformer features a relatively small magnetic path length in relation to the amount of leakage flux, the simulated values for the model without flux leakage will broadly coincide with the results of the model with flux leakage.

The last part of Chapter 5 demonstrates the use of a capacitor in parallel with the secondary winding of the transformer in order to produce a demagnetizing current that counteracts the magnetizing current and in consequence boosts the output power. A model is derived for this case as well as the principles of operation of the complete equivalent circuit, with emphasis in adequately sizing the capacitor for various simplifications.

Additional load tests are performed in order to measure the impact of using the capacitor to increment the output power of the transformer and therefore avoid increasing the core size as a means to increase the power delivered to the load. After experimentally reaching the optimum capacitor value for the long UI transformer ($C = 185$ μF), the results show that the maximum output power retrieved for this case is $P_{o_{max}} = 635$ W, hence there is an increase of around 17% in the output power of the transformer in relation to the case without the capacitor.

6.2 Future Work

The work performed throughout this thesis allowed the validation of transformer models and the establishment of an associated design procedure. Given the lack of materials, it was not possible to build a new transformer designed through these methods. Therefore, forthcoming work should be focused on applying the design method and building a new transformer with a high grade silicon steel.

Since the transformer is an important component of the power supply, the fundamental and practical limitations thereof establish the success of the overall system. Hence, a careful design following strict limitations has to be carried out. This can be done by looking at the output power as a function to maximize with degrees of freedom such as the effective cross-section of the core and the length of the core, while being subjected to a series of limitations and constrains that originate from the general specifications, such as the transmission line current, the necessary window size and the weight limit. A solution with the dimensional data of the new transformer can then be found with this iterative process and be subsequently implemented.

This thesis as shown the material and its properties are influential in the viability of the transformer, which is typically measured by the magnitude of the output power. Consequently, the new transformer has to be implemented in a silicon steel of higher grade than that of the analysed transformers in this thesis. The magnetic permeability is a key factor in the magnitude of the output power and should be as high as possible since the transformer is operating in saturation, a region were the magnetic permeability is significantly decreased in relation to it's maximum value.

Lastly, the application of a capacitor to the secondary winding of a transformer has shown potential through the results obtained in this thesis. This enhancement to the power supply of the RIOL can be investigated in more detail in order to measure the effect on other transformers as well as clarify and fine tune the procedure to achieve the optimum capacitor value with more precision. This endeavour should be done through the improvement of the field data available for each transformer, since the parameters of the transformer are necessary to the models that design the capacitor.

Bibliography

[1] J. Sawada, K. Kusumoto, Y. Maikawa, T. Munakata, and Y. Ishikawa, "A mobile robot for inspection of power transmission lines," Power Delivery, IEEE Transactions on, vol. 6, no. 1, pp. 309–315, Jan. 1991.

[2] S. Peungsungwal, B. Pungsiri, K. Chamnongthai, and M. Okuda, "Design considerations for series-connected distributed FACTS converters," Circuits and Systems, The 2001 IEEE International Symposium on, vol. 3, pp. 121–124, Jun.-Sep. 2001.

[3] L. Tavares and J. Sequeira, "RIOL - robotic inspection over power lines," Procs. of the 6^{th} IFAC Symposium on Intelligent Autonomous Vehicles, IAV, no. 1, Sep. 2007.

[4] H. Zangl, T. Bretterklieber, and G. Brasseur, "A feasibility study on autonomous online condition monitoring of high-voltage overhead power lines," Instrumentation and Measurement, IEEE Transactions on, vol. 58, no. 5, pp. 1789–1796, May 2009.

[5] ——, "Energy harvesting for online condition monitoring of high voltage overhead power lines," Instrumentation and Measurement Technology Conference Proceedings, 2008. IMTC 2008. IEEE, pp. 1364–1369, May 2008.

[6] S. Peungsungwal, B. Pungsiri, K. Chamnongthai, and M. Okuda, "Autonomous robot for a power transmission line inspection," in Circuits and Systems, 2001. ISCAS 2001. The 2001 IEEE International Symposium on, vol. 2, 6-9 2001, pp. 121–124.

[7] D. D. N. de Mesquita Furtado Lopes, Transformador para Robot de Inspecção de Linhas Aéreas, MSc. Thesis, Instituto Superior Técnico, Lisboa, Portugal, October 2011.

[8] H. Johal and D. Divan, "Design considerations for series-connected distributed FACTS converters," Industry Applications, IEEE Transactions on, vol. 43, no. 6, pp. 1609–1618, Nov. 2007.

[9] C. W. T. McLyman, Transformer and Inductor Design Handbook. New York: Marcel Dekker, Inc., 2004.

[10] R. Aggarwal, A. Johns, J. Jayasinghe, and W. Su, “An overview of the condition monitoring of overhead lines,” Electric Power Systems Research: An International Journal, Elsevier Science, vol. 53, pp. 15–22, 2000.

[11] S. Abraham, National Transmission Grid Study, U.S. Dept. Energy, Washington, DC, 2002.

[12] N. Tanaka, World Energy Outlook 2008, International Energy Agency, Paris, 2008.

[13] D. M. Divan, W. E. Brumsickle, R. S. Schneider, B. Kranz, R. W. Gascoigne, D. T. Bradshaw, M. R. Ingram, and I. S. Grant, “A distributed static series compensator system for realizing active power flow control on existing power lines,” Power Delivery, IEEE Transactions on, vol. 22, no. 1, pp. 642–649, Jan. 2007.

[14] F. A. Silva, J. Caxias, and J. Sequeira, “Transmission line inspection robots: Design of the power supply system,” 2008.

[15] A. de Souza, L. A. Moscato, and et al., “Inspection robot for high-voltage transmission lines,” Mechatronics, The ABCM Symposium Series on, vol. 1, pp. 1–7, 2004.

[16] H. San Segundo, V. Fuster, L. Perez, and P. Mayorga, “Automated inspection of electric transmission lines: The power supply system,” nov. 2006, pp. 3788–3792.

[17] J. M. Barnard, J. A. Ferreira, and J. D. van Wyk, “Sliding transformers for linear contactless power delivery,” Industrial Electronics, IEEE Transactions on, vol. 44, no. 6, Dec. 1997.

[18] A. Fitzgerald, C. Kingsley, and S. Umans, Electric Machinery, ser. Electrical Engineering Series. McGraw-Hill Companies,Incorporated, 2003.

A

Appendices

A.1 Laboratory apparatus to obtain the primary current

Ideally, the load tests that were devised for the transformers described in Chapter 4 would require a primary current that could vary from 100 to 1000 A *rms* in order to match the transmission line current. However, that goal could not be achieved from the low voltage grid outlet, with the existing equipment in the laboratory.

A previous work in the area managed to retrieve a peak current of 300 A (around 212 A *rms*) through the use of three auxiliary transformers [7]. In this thesis, the laboratory set-up was altered by substituting two of the previous auxiliary transformers with one different transformer as shown in Figure A.1. With this change it was then possible to generate a *rms* current varying from 0 to 350 A for use as the primary current of the tested transformer.

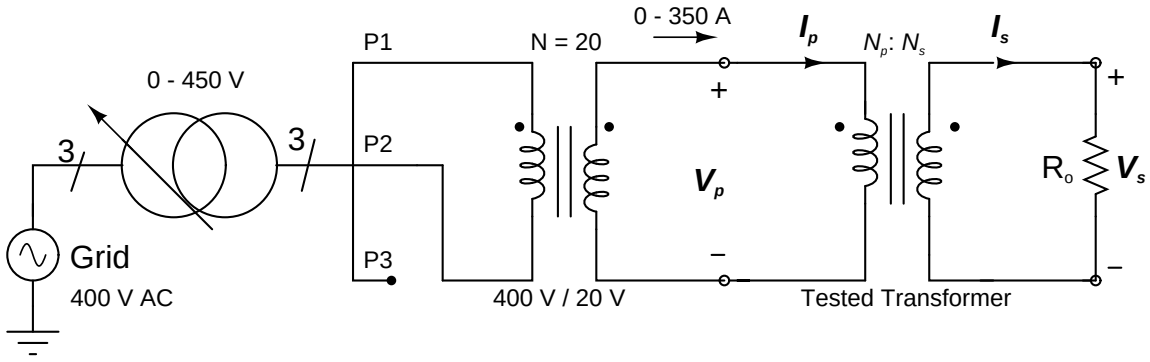

Figure A.1: Laboratory set-up for the load tests.

The three phases from the grid are connected directly to an autotransformer, that regulates from 0 to 450 V, which is used to manage the level of the primary current injected into the tested transformer. Afterwards, two phases are drawn from the autotransformer and feed to a step-down transformer with a ratio of 20, $400/20$ V, that will elevate the current that is then passed on directly to the tested transformer.